university of groningen

faculty of science and engineering

Disentangling the Cosmic Web: angular perspective on dynamics of cluster environments with spherical harmonics

Author:
Kasia LELONEK
(s4733916)

Supervisor:
prof. dr. M.A.M. (Rien) VAN DE WEIJGAERT
Second examiner :
prof. dr. Diederik ROEST

Bachelor's Thesis
To fulfill the requirements for the degree of
Bachelor of Science in Physics
at the University of Groningen

July 25, 2024

Contents

Page

Abstract **3**

Acknowledgements **4**

1 Introduction **5**
1.1 Discovering the Cosmic Web 5
1.2 Clusters' perspective: outline and predictions 7

2 Large-scale dynamics of structure formation **8**

3 The Illustris dataset **11**

4 Methods **13**
4.1 Delaunay Tessellation Field Estimator 13
4.2 HEALPix (Hierarchical Equal Area isoLatitude Pixelation) 14
4.3 Spherical harmonic analysis 16

5 Mass distribution around cluster nodes: visual assessment **18**
5.1 A case study of a single cluster 20
5.2 A comparative study of an array of diverse cluster environments 22

6 Mass distribution around cluster nodes: spherical harmonic analysis **26**
6.1 A case study of a single cluster 26
6.2 A comparative study of an array of diverse cluster environments 29

7 Mass flow around cluster nodes **32**
7.1 Visual evaluation 32
7.2 Contributions from filaments and voids 34

8 Summary of main contributions **38**

9 Conclusion **40**
9.1 Outlook 40

Bibliography **42**

Appendices **46**
A Appendix A: Cosmic Atlas 46
A.1 Cluster 1 46
A.2 Cluster 2 48
A.3 Cluster 3 50
A.4 Cluster 4 52
A.5 Cluster 5 54
B Filament and void contribution to matter flow 56

Abstract

The problem of mass distribution and flow within the Cosmic Web, a large-scale foam-like structure of walls, filaments, clusters, and voids formed by the distribution of matter throughout the Universe and shaped by gravitational instability and tidal forces, is addressed. The investigation focuses on the clusters and the environment around them seen from an angular perspective, which offers a view into the connectivity and hierarchy in the context of large-scale structure. Clusters, lying at the intersection of a web of filaments, are also the most relevant mass-accreting elements of the Cosmic Web, and provide an insight on the large-scale mass migration. The approach is complemented by a Cartesian overview of the wider structure.

The mass distribution was drawn from the Illustris-3-Dark simulation and illustrated using HEALPix projection histograms. The resulting maps were analyzed using spherical harmonics analysis by extracting the power series coefficients, illustrating the reconstructed maps, the residues of the maps upon subtracting the spherical structures, and the power spectra. The results strongly indicate the existence of substructure within the distribution, with more massive clusters indicating more complexity in their environment. It is also confirmed that cluster's mass correlates to the number of incoming filaments. Flux around clusters was inferred based on the differences of mass distribution plots as well as visual examination of the velocity field and proved filaments to provide most of the incoming mass, with the magnitude of the contribution increasing in time. Meanwhile, voids were found to have a contribution significantly smaller and diminishing over time, assigned to the erasure of substructure in their merging process and subsequent loss in density.

Acknowledgments

With my three-year journey coming to an end, the process of writing this thesis brings closure to a beautiful chapter in my life, one that I will be grateful for for years to come. If I were to do all the people who made this work possible justice, I think the resulting text would be longer than my report. Nonetheless, I will try my best.

Firstly, I must express my thanks to Rien van de Weijgaert, who supervised me through this process. He created a wonderful research group for us Bachelor students and made the past two and half months a fulfilling journey, where I felt supported and assured. A huge thank you is also in order to Aleksandra Biegun, who has been an overwhelming support throughout the last two years. She is my role model and brought me so much of the inspiration and motivation that helped me get to this point.

The three years in Groningen were also marked by so many friends, more than I could count. I would like to thank everyone who sat with me at the Hydra room every day, their company offered a huge relief in times of stress, and their expertise was always appreciated in the often frustrating process of writing code. I am grateful to the people I spent almost every day with, Matthieu, Tunay, and Petra, and to those I saw less often, especially Moritz. They introduced so much fun and beautiful moments into my life.

I moved here from Poland with two guys that mean the world to me, Kuba and Karol. The last six years were a ride. I wouldn't be here today, finishing a degree, without their support and love.

Lastly, a huge thank you to Alex and my parents.

1 Introduction

Yakov Zeldovich, a Soviet cosmologist know for his work on large structure formation, compared it to Freud's theory of psychoanalysis where behaviours in adults stem from childhood experiences [1]. In a similar vein, the largest scale structure, baptised the Cosmic Web [2], began forming when the Universe was in its cradle, with density fluctuations in the primordial soup. The expansion that followed took the quantum noise to astrophysical scales which became the canvas for gravity to create ever more complex structures.

From the resulting foam-like entity emerges a substructure of walls, filaments, clusters, and voids [3]. Its pattern can be observed on scales up to 100 Mpc, beyond which the Universe appears homogeneous in accordance with the Cosmological Principle [4], [1]. The Cosmic Web hosts dark matter halos facilitating galaxy formation. Those clusters occupy a space spanning around 1-3 h^{-1} Mpc, while the connecting filaments are typically less than 10 h^{-1} Mpc long. The space between them forms voids, under-dense regions where galaxies are few and far between [5].

Clusters and their environments form a unique probe for the Cosmic Web dynamics, allowing the determination of cosmological parameters and amplitudes of initial density fluctuations in the early Universe, all while being easily identifiable. The other extreme, the voids, can be seen as a complementary tool. Computing the power spectra of clusters is one of the first possible steps to inferring crucial observations about the early Universe [6].

Those regions can be probed from an angular perspective, meaning the view of the surrounding structure is presented as a sphere seen from the center of a cluster. The treatment offers insight into the connectivity between different elements of the Cosmic Web on multiple scales, revealing the intricacies of the structure. Moreover, such view allows straight-forward identification of the types of surrounding morphological elements, their number, and their relation to each other. The exterior structure around the clusters is also one of the factors defining the mass migration around it, granting an insight into the connection between the two. The approach was first proposed by Villumsen and Davis, who investigated the velocity fields around clusters, with a focus on the Virgo Superclustser, motivated by modelling the asphericity of the mass inflow for a number of clusters [7]. The following work elaborated on the nature of the influx and its relationship to the surrounding structure, which can be seen as an extension upon the aforementioned work.

The power spectra, besides the insight into cosmological parameters, also shine light on the substructure of the examined region. While many studies focus on the substructure in the voids, other Cosmic Web environments are yet to receive such in-depth treatment. The aim of the following study is to provide a insight on connectivity and substructure by centering the clusters in angular view and conducting spherical harmonic analysis of the mass distribution as well as investigating mass migration seen from this unique perspective.

1.1 Discovering the Cosmic Web

The idea of large-scale distribution of galaxies can be traced back to Edwin Hubble who, based on the Shapley-Ames catalogue, concluded that galaxy distribution is non-uniform on smaller scales but follows Poisson statistics on larger ones. The sentiment further crystallised in the 60s and 70s with the help of a number of maps created based on the Lick catalogue which showcased the richness of

the structure [8], [9].

In the following years, based on multiple surveys including Lick, Jim Peebles published a series of articles showing that the two-point correlation function exhibits power law-like behavior on smaller scales [10]. Those findings contributed to further research in the field of large-structure observations with another breakthrough in 1982, where the roots of the contemporary understanding of the Cosmic Web began with Adrian Webster analysing the spatial distribution of quasars and noticing a pattern on scales larger than ever though before [5], [11].

Current findings about the structure of the Universe are drawn from increasingly sophisticated observational data. One of the utilised methods requires deep redshift surveys implementing spectroscopic methods [12]. A popular example is the Sloan Digital Sky Survey (SDSS), containing thousands of galaxies, from which images highlighting the peculiar pattern, such as figure 1, can be obtained.

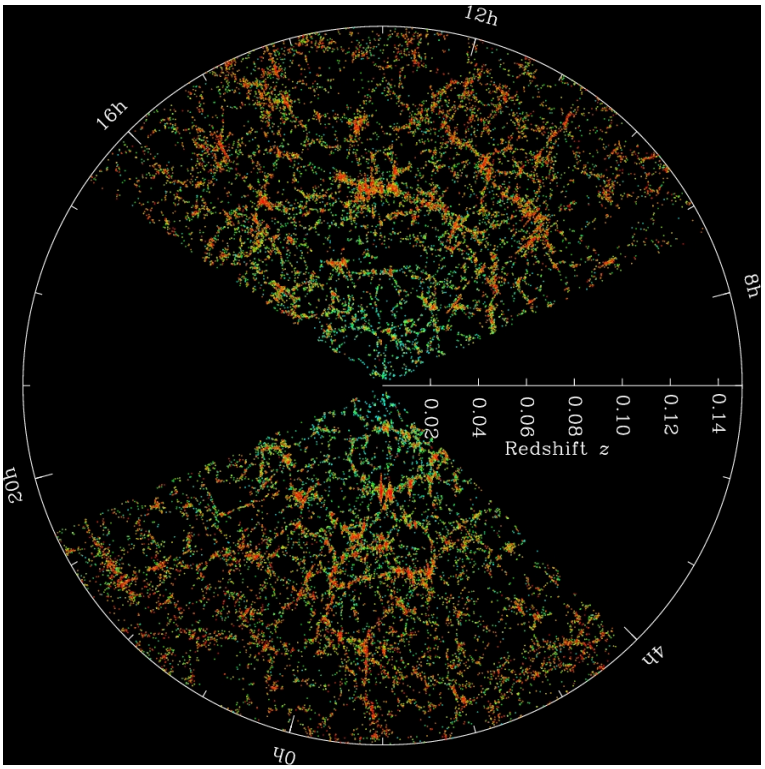

Figure 1: An example of a map produced using the SDSS with Earth at the center. The presented galaxy distribution shows a clear, web-like pattern. Image courtesy Michael Blanton and the Sloan Digital Sky Survey team.

Another pillar on which large-scale structure research is based is the Lyman-α forest, sourced to quasars and intergalactic gas. This collection of absorption lines in the Lyman series of hydrogen, if of cosmological origin, can offer insight into the cosmic density field and be a powerful cosmological probe [13]. One of the most recent developments in the observational sphere is DESI, the Dark Energy Spectroscopic Instrument, which has first started working in 2019. The spectograph covers redshifts of up to $z = 35$ and investigates a range of around 22 million galaxies, providing exceptional insight into the Lyman-α forest and putting new constraints on our cosmological models and unlocking a state-of-the-art view on large-scale structure [14], showcased in figure 2.

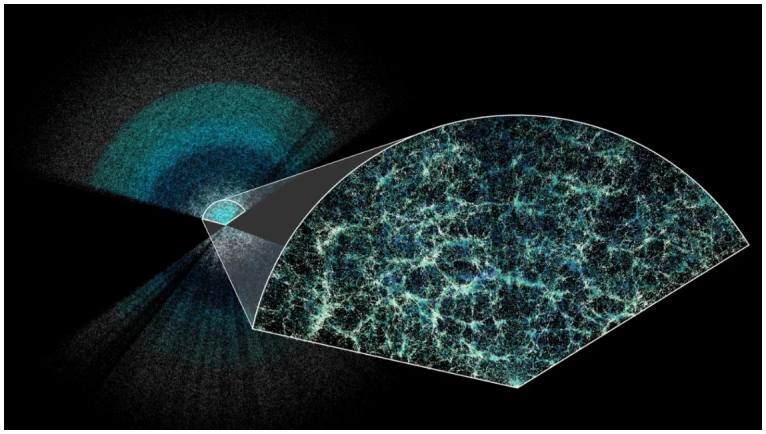

Figure 2: Selected detail from the DESI map showcasing the large-scale structure of the Universe. Image courtesy Claire Lamman/DESI Collaboration [15]

The observations are complemented by N-body simulations, where a large number of massive particles is used to model the Cosmic Web. An initial cosmological model and the laws of gravity dictate how the particles evolve through time [16]. The Illustris project is one of the open-access providers of such simulations in a variety of resolutions in both baryonic and purely dark matter versions. The latter, which is the backbone of the following investigation, cannot pose predictions on the baryonic components of the universe, but is a basis for the large structure formation [17].

Together, the observational and simulated data, successfully paint a coherent picture of the large-scale structure. The current view of the Cosmic Web provides insight into not only the mechanisms governing the universe now, but also puts constraints on the possible inflation scenarios [13]. Hence, the holistic study of universal dynamics is crucial to modern science, as it addresses issues at the crossroads of cosmology, astrophysics, and physics.

1.2 Clusters' perspective: outline and predictions

The following investigation focuses on the distribution and flow of matter within the Cosmic Web based on the environments around massive clusters viewed from angular perspective. Chapter 2 outlines the mechanism and proceedings of cosmic structure formation, including the details of how matter flows within given structures. Chapter 3 outlines the details of the dataset based on which the problem was analyzed, while Chapter 4 describes the methods used, including, Delaunay Tessellation Field Estimator, HEALPix histograms and spherical harmonic analysis. Chapters 5 and 6 showcase the findings by means of visual and spherical harmonic analysis respectively. The two chapters are separated into a detailed case study of a single cluster and a comparative study of four other clusters, forming a coherent picture of mass distribution. The problem of mass flow is addressed in Chapter 7, where the contributions of filaments and voids are detangled. Lastly, a complete summary, conclusions, and outlook can be consulted in Chapters 8 and 9.

It is expected that that both filaments and voids will have a contribution to the inflow of matter into clusters. Most of the matter is speculated to arrive through filaments, though the voids might be more significant then previously thought. Despite their low density, they are the ingredients of largest volume in the Cosmic Web, which would justify such proposition.

2 Large-scale dynamics of structure formation

Interactions on the largest scale are dominated by gravity, with their proceedings being dictated by the gravitational instability theory and cosmic tidal forces. The two phenomena, constantly at interplay, shape the formation and the current dynamics of the Cosmic Web, giving insight, among others, into mass migration mechanisms [18], [19].

The gravitational instability theory, described by Zeldovich, states that the present-day large scale structure is a result of small density fluctuations in the largely homogeneous early Universe [18]. According to his findings, inhomogeneous distribution of matter must collapse along a single axis due to the gradient of the particular velocity in a system becoming too large to sustain the shape, leading to formation of "Zeldovich pancakes" seen in figure 3. The pancakes crossing each other lead to structure formation, which takes place as the density contrast, or the ratio between density in a volume and mean density of the local universe [20], reaches the order of $\frac{\delta\rho}{\rho} \simeq 1$ and the density fluctuation are no longer defining the expansion [21].

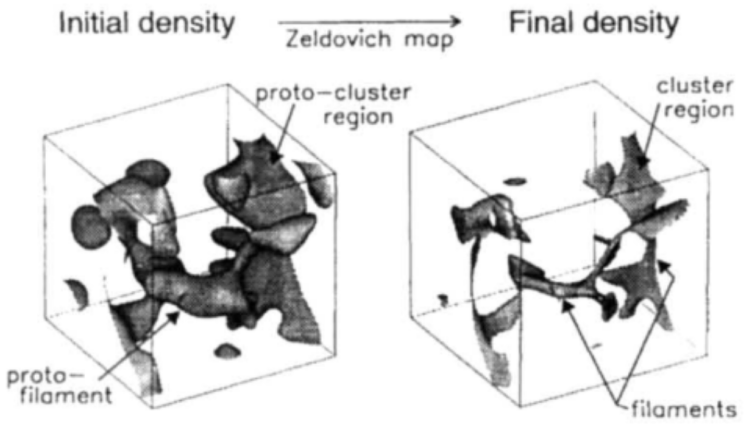

Figure 3: A density field based on ΛCDM primordial density distribution (left) and the densities resulting from a Zeldovich map (right) [18].

The primordial density fluctuation field, in the ΛCDM cosmology, is given by a random Gaussian distribution. Within the model, the evolution of collision-less, self-gravitating dark matter can be described by the Vlasov-Poisson equations (1) given below. They are also the starting point for deriving the continuity equation and Eulerian equations of motion. The subsequent investigation is based on a simulated universe, composed exclusively of dark matter and energy, evolving according the established model.

$$\begin{cases} \partial_t f + \frac{\mathbf{p}}{ma^2} \cdot \nabla_{\mathbf{x}} f - \nabla_{\mathbf{x}} \phi \cdot \nabla_{\mathbf{p}} f = 0 \\ \nabla^2 \phi = 4\pi G a^2 (\rho - \rho_b) \end{cases} \tag{1}$$

Here, ϕ is the gravitational potential, f is the distribution of particles, $\mathbf{x}$ is expressed in comoving coordinates and $\mathbf{p}$ is its conjugate variable, ρ_b is the mean mass density, and ρ is given as [22]:

$$\rho(\mathbf{x},t) = \frac{m}{a^3} \int f(\mathbf{x},\mathbf{p},t) d\mathbf{p}$$

Effectively, the equations imply that the temporal change in particle distribution is dictated by the difference between the product of spatial gradient of gravitational potential and gradient of the distribution in momentum space, and the spatial gradient of the distribution. At the same time, the potential follows from the relative density within a given system. As such, equations 1 give some hints at a hierarchy in flux contributions according to types of structure, however, the exact details would require solving them for a concrete system.

On larger scales, the mechanism of gravitational instability implies that walls are formed first, followed by filaments, and finally clusters. Since mass in less dense environments is attracted towards the denser ones, it creates a runaway-like mechanism, with dense regions becoming denser, and hence, attracting even more material. Effectively, this leads to concluding that the mass within a system flows in a specific order; out of voids, through walls to filaments, and through filaments to clusters. It is further implied that, in general, voids will always loose material and clusters will always gain it, while walls and filaments experience a more complex flux, with a constant inflow and outflow [23], [24]. Such cosmic flow can be deduced by investigating the associated velocity field. An example of the results of such endeavour is highlighted in figure 4, and is in agreement with the hypothesized flow [25].

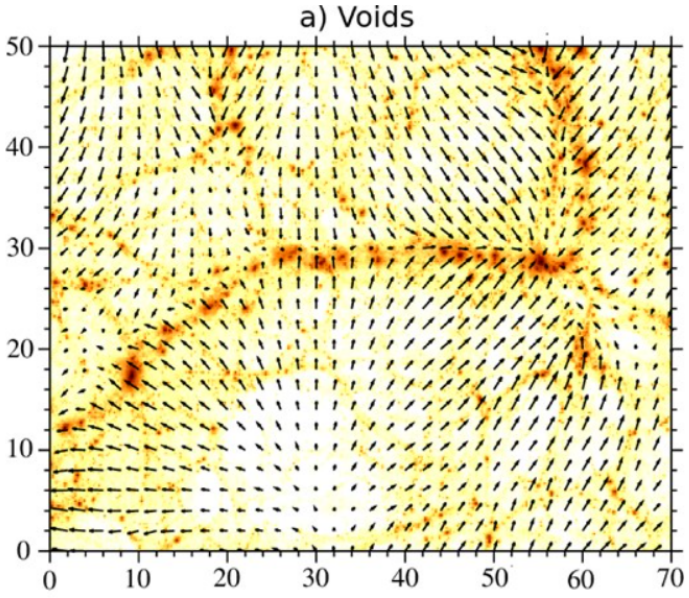

Figure 4: The velocity field of a void region. The most under-dense regions show outflow of matter through diverging field lines, while the filamnets show a flow towards the cluster. Some contribution of voids directly to the clusters is visible [25].

The formation of the Cosmic Web is driven further by the tidal forces caused by the inhomogeneous mass distribution introduced by the gravitational instability. The result is an asymmetry between the magnitude of the gravitational force within a body, stimulating cosmic structure formation. The anisotropy fuels the gravitational instability further, and vice-versa, creating a feedback loop resulting in a web-like structure [19].

The two structures that are of concern in the following investigation are filaments and voids. In the earlier universe a vast, complex network of thin filaments can be distinguished. With time, those

structures merged to form more massive, thicker ones, while creating more pronounced voids, evident from the proto-filaments to the ones seen today being identifiable at higher redshifts [24]. Like filaments, voids also evolve to merge together under the influence of the tidal forces, becoming more spherical and less dense [26]. The two differ when considering their mass over the course of their evolution; voids seem to deflate, while filaments retain a steady amount over longer times [27]. At the same time, the clusters are considered to have formed rapidly to now contain a significant fraction of the total mass in the Cosmic Web. Little changes have been observed in those structures at times more recent than $z = 0.5$, which suggest the examined sample should cover higher redshifts [25].

Based on the outlined theory of structural dynamics, it is expected that the mass distribution around clusters will include filaments dominating at the closest scales, since the nodes are embedded within them. When extending the view to larger distances, walls might also show a contribution. The inflow, according to the order set by the gravitational stability theory and tidal forces, should be sourced predominantly to filaments. A certain contribution is expected to be incoming from the voids directly. However, as they become less massive and dense with time, they will not be able to supply a sustained influx.

3 The Illustris dataset

Observational data is complemented by N-body simulations with a large number of massive particles used to model the Cosmic Web, where an initial cosmological model and the laws of gravity dictate how the particles evolve through time [16]. Such treatment becomes necessary as the cosmic dynamics become non-linear, and hence, can no longer be described by analytical solutions. The Illustris project [28], [17] is one of the open-access providers of such simulations in a variety of resolutions, in both baryonic and purely dark matter versions. The latter was chosen for the purpose of the following investigation as it is a basis for the large structure formation, however, it does not allow forming predictions on the baryonic components of the universe [17].

Illustris is a cosmological hydrodynamical simulation based on AREPO. The principle on which the method is built relies on solving hyperbolic conservation laws of ideal hydrodynamics on a moving, unstructured mesh of Voronoi tessellations, which take a form of space-filling triangles or tetrahedra, depending on the dimensions of the problem. The advantage of such approach over preceding methods, such as Lagrangian smoothed particle hydrodynamics or Eulerian hydrodynamics on a Cartesian grid, is that it unites highly accurate treatment of self-gravity with high resolution collisionless dark matter, while avoiding distortions introduced by other, static grids [29].

The Illustris project was motivated by the idea of a highly detailed dataset that is accurate on cosmological scales that is able to resolve the internal structure of individual galaxies. The result is contained within 265 TB of disk space, available in API and HDF5 formats, which contain gas cells, passive gas tracers, stars, stellar wind particles, supermassive black holes, and dark matter particles. The richness of the offered data is illustrated in figure 5.

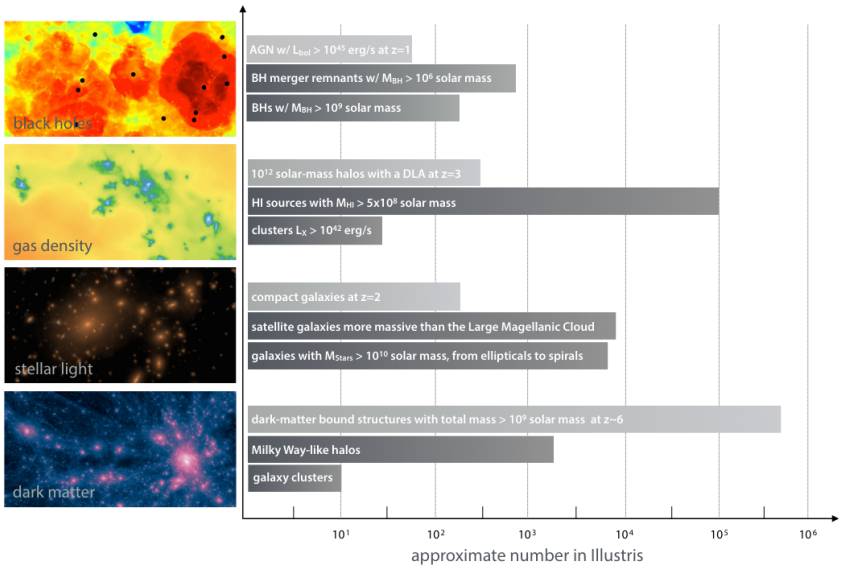

Figure 5: A visualisation of the data available within the Illustris simulation [17].

The available data is organised in three options, where Illustris-3-Dark is the lowest resolution one. It contains 455^3 dark matter particles, each with a mass of $4.8 \times 10^8 M_\odot$. They occupy a periodic, 106.5 Mpc-long box and are sorted by a Friends-of-Friends algorithm rather than their position in space [17], [28]. The parameters chosen for the simulation are based on the WMAP-9 data, with dark

matter density of 0.2726, dark energy density of 0.7274, and Hubble constant (given as ”little h”) h = 70.4 km/s/Mpc. The aforementioned resolution option was chosen due to the low computational load it offers, while remaining highly accurate.

The entirety of data obtained from Illustris is highlighted in figure 6. Three slices through the entire box are presented, exhibiting the web-like structure.

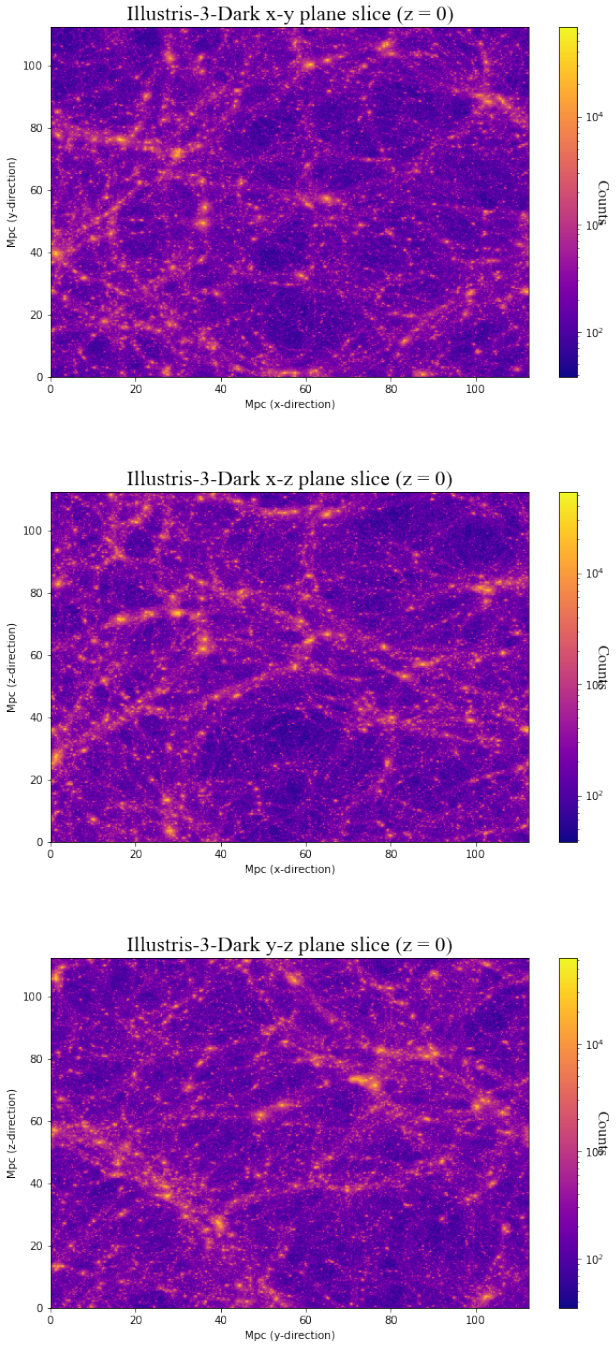

Figure 6: Illustris-3-Dark mass distribution illustrated in three two-dimensional slices.

4 Methods

The issue of mass distribution and migration within the large-scale structure is addressed from angular perspective, and hence necessitates a toolkit specific to treatment of spherical functions. The Delaunay Tessellation Field Estimator is used as a starting-point visualization tool, highlighting the richness of examined structure through mass distribution plots defined on a Cartesian meshgrid, before examining the angular case.

The problem of angularity is addressed using HEALPix, a 2-sphere projection designed for analyzing data using spherical harmonic functions. The mechanism behind the method involves dividing the sphere into equal-area quadrilaterals, which facilitated the creation of mass distribution maps based on a simple histogram approach, solving the issue of determining densities defined on a sphere, as in the angular view of the Cosmic Web from the clusters' perspective.

The quantitative analysis of the cosmic environments was conducted through spherical harmonic analysis. Those functions can be viewed as a Fourier transform defined on a sphere, which allows decomposition of the data into specific components, such as, but not limited to, monopole, dipole, or quadrupole contributions, the latter corresponding to filamentary structures.

4.1 Delaunay Tessellation Field Estimator

The data provided by the Illustris simulation was analyzed using the Delaunay Tessellation Field Estimator (DTFE) developed by Schaap and van de Weygaert [30], [31]. Delaunay tessellations, taking the form of triangles for two dimensional spaces, form a backbone for the method. A circumcircle can be ascribed to each of the space-filling triangles such that it does not contain any other points on the grid besides the "seed", or the point that was used to generate the shape, of a given triangle. Dividing the space this way leads to maximizing the minimum angle for every triangle, creating optimization properties which are exploited in the algorithm [32], [33], [34]. Moreover, DTFE is volume-weighted, as opposed to other, more widespread mass-weighted methods, making it preferable for velocity fields, which are used to illustrate the mass flow [35].

DTFE was applied to a set of points defined in the Illustris simulation, where scales of up to 22.5 Mpc per side was treated. The values of density and velocity were evaluated on a regular meshgrid. An example of a density map achieved this way can be seen in figure 7

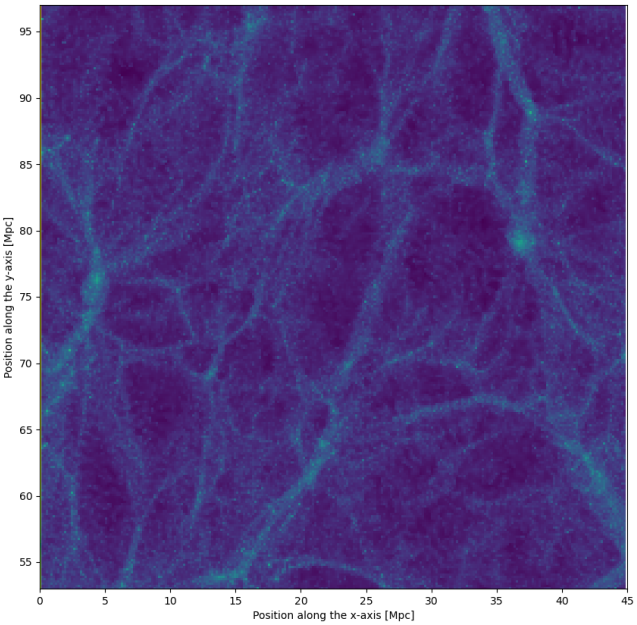

Figure 7: Example of a density map created using DTFE based on a 45 Mpc-long slice through the Illustris-3-Dark simulation.

Ultimately, the use of DTFE was limited to visualisation purposes. The investigation of the mass distribution and flow from clusters' perspective requires the implementation of a spherical coordinate system, which is not compatible with the algorithm's rectangular grid. A possible solution to the problem would be to employ an interpolation of the values from the mesh to points on a sphere, however, this approach would introduce significant distortions, and hence, was discarded as a viable option in favor of the HEALPix alternative.

4.2 HEALPix (Hierarchical Equal Area isoLatitude Pixelation)

With the development of observational techniques arose the challenge of processing large amounts of astronomical data collected over the whole sky. One of the solutions, originally motivated by the Cosmic Microwave Background (CMB) research, is the Hierarchical Equal Area isoLatitude Pixelation (HEALPix) algorithm designed by Krzysztof Górski in 1998 [36]. An example of implementation of Górski's method to CMB is illustrated in figure 8, where a map and its power spectrum are included. The ensuing investigation was inspired by such analysis applied in the context of cluster environments.

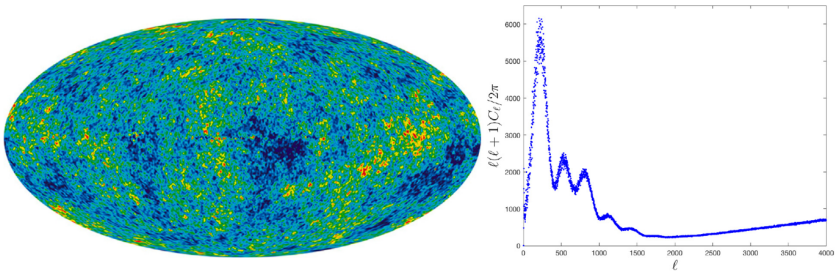

(a) (b)

Figure 8: An example of a HEALPix map - a view of the Cosmic Microwave Background (a) and the corresponding power spectrum (b) [37].

In Górski's approach, a sphere is partitioned into equal area quadrilaterals, each of different shape, as highlighted in figure 9. This treatment facilitates high-resolution discretisation of functions on a sphere while minimizing the systematic error introduced by discrete spherical harmonic decomposition [38]. HEALPix integrates cylindrical equal-area and Collignon projections, depending on whether the equatorial or the polar region is sampled, naturally leading to a diamond-like projection structure [39].

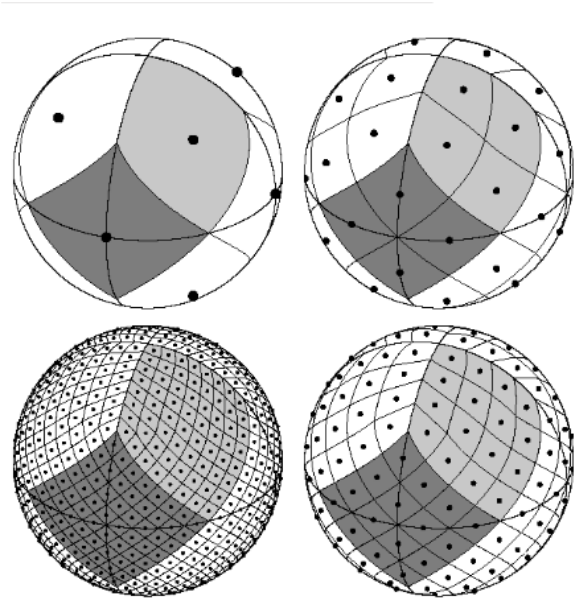

Figure 9: HEALPix grid with resolution increasing clockwise from top-left image. Dark grey represents an example of the division in the equatorial region and light grey of the polar region [36].

Three main requirements for discrete sky maps have been formulated and answered by Górski et al: hierarchical structure of the data base, equal areas of discrete elements of the partition, and iso-latitude distribution of the elements on the sphere. The hierarchy of the database ensures the points located in proximity to each other in the map are also stored nearby, optimizing the RAM usage. Equal area partition ensures the white noise from the observational instrument and the pixel space is merged and the sky is sampled equitably. Lastly, the iso-latitute distribution of the elements is the most relevant to the following investigation, as spherical harmonic decomposition requires computing the associated Lagendre polynomials, which necessitates recursion. The implemented distribution ensures fast

analysis of functions defined on a sphere.

The structure of the data in a HEALPix map involves the N_{side} parameter and ordering. The variable dictates the number of divisions along the side of a base resolution pixel and hence, the resolution. Ordering can be divided into two schemes. In the ring scheme, the pixels are read and numbered from north to south along each iso-latitude, which is most suitable for spherical harmonic analysis. Nested ordering is a tree-like structure, which allows easy nearest neighbour search and will not be the focus of the investigation [38].

4.3 Spherical harmonic analysis

Just as functions defined in Cartesian coordinates can be decomposed into frequency-specific components through Fourier series, data described on a sphere can be discerned through a spherical harmonic series. The investigation of the Cosmic Web environments is conducted from an angular perspective, resulting in spherically-defined data, with the goal of evaluating the prominence and number of specific structures in the environment of a given cluster, for instance the filaments. As such, the problem calls for implementation of spherical harmonic analysis, which facilitates such treatment by allowing a quantitative description of the mass distribution overall, while revealing the details of the structure.

Spherical harmonics are polynomials arising from solving Laplace's equation (2) in spherical coordinates [40], [41].

$$\nabla^2 f = \frac{1}{r^2}\frac{\partial}{\partial r}\left(r^2\frac{\partial f}{\partial r}\right) + \frac{1}{r^2\sin\theta}\frac{\partial}{\partial\theta}\left(\sin\theta\frac{\partial f}{\partial\theta}\right) + \frac{1}{r^2\sin^2\theta}\frac{\partial^2 f}{\partial\varphi^2} = 0 \tag{2}$$

The ordinary partial differential equation (2) can be separated into radial, azimuthal, and polar components. Treating the azimuthal component first yields the following solutions:

$$\frac{1}{\Phi(\varphi)}\frac{d^2\Phi(\varphi)}{d\varphi^2} = -m^2 \Rightarrow \Phi(\varphi) = e^{-im\varphi}, e^{im\varphi} \tag{3}$$

The matter becomes more complex for the polar component, where the solutions include Legendre functions. They take the form given by equation 4.

$$\Theta(\theta) = \sqrt{\frac{2n+1}{2}\frac{(n-m)!}{(n+m)!}}P_n^m(\cos\theta) \tag{4}$$

Where $P_n^m(\cos\theta)$ is the Lagendre function

$$P_n^m(\cos\theta) = \frac{1}{2^n n!}\left(1-x^2\right)^{m/2}\frac{d^{m+n}}{dx^{m+n}}\left(x^2-1\right)^n$$

Finally, collecting the two solutions in equations 3 and 4 yields the spherical harmonics in equation 5 [42].

$$Y_n^m(\theta,\varphi) \equiv (-1)^m\sqrt{\frac{2n+1}{4\pi}\frac{(n-m)!}{(n+m)!}}P_n^m(\cos\theta)e^{im\varphi} \tag{5}$$

When examining functions defined on a sphere, the spherical harmonics can be summed in a series equivalent to a Fourier transform.

$$\widehat{f}(\theta_i,\phi_i) = \sum_{\ell=0}^{\ell_{\max}} \sum_{m=-\ell}^{\ell} a_\ell^m Y_\ell^m(\theta_i,\phi_i), i = 1,\ldots,N \tag{6}$$

In equation 6 above, $\widehat{f}$ is the approximated function and a_ℓ^m are the coefficients in the series given by equation 7, where f is the original data.

$$a_\ell^m = \frac{4\pi}{N} \sum_{i=1}^{N} \bar{Y}_\ell^m(\theta_i,\phi_i) f(\theta_i,\phi_i), 0 \le \ell \le \ell_{\max}, -\ell \le m \le \ell \tag{7}$$

From the above, the power spectrum can be obtained based on the coefficients C_ℓ defined in equation 8 [37].

$$C_\ell = \frac{1}{2\ell+1} \sum_m |a_\ell^m|^2 \tag{8}$$

5 Mass distribution around cluster nodes: visual assessment

The distribution of mass from the clusters' perspective was determined using the HEALPix approach implemented through the healpy python package, developed specifically for processing pixelated data on a sphere. To ensure compatibility, the points were defined on a 2-sphere. The projection was achieved by converting the points extracted from the Illustris simulation from Cartesian to spherical coordinates and eliminating the radius as a variable. Such procedure was done for radii of 5 and 10 Mpc away from the center of each cluster. Considering that the clusters themselves cover a radius of around 1-3 Mpc [5], such choice ensured the surrounding structure was captured. Subsequently, the density was determined by treating each HEALPix pixel as a histogram bin and counting the number of particles within each partition. The resulting maps were plotted in Mollweide projection, which allows the structure of the Cosmic Web to be distinguished visually, where filamentary elements take the form of spherical hot spots, usually having a partner reflecting the incoming and outgoing filaments, and walls can be seen as fainter, but still distinct, rings or other elongated structures.

For additional visual overview, the mass distribution was also plotted in Cartesian coordinates. The scales involved extend up to 22.5 Mpc, which tests the limit of the Illustris-3-Dark resolution when using the histogram approach adapted for the spherical case, as the filamentary structures become disconnected, and would require a degree of smoothing to become identifiable again. To resolve the issue, DTFE was chosen to visualise the density of the environment, due to its advantage in recognizing filaments despite the relatively low data resolution. As the Cartesian view is included as a supplementary visualisation tool, it is limited to a single slice through each cluster.

The locations of clusters selected for the ensuing analysis are highlighted in white, numbered boxes in figure 10. Those particular regions were chosen with the aim of creating a sample of diverse cluster environments, where two are some of the most massive objects within the whole structure, and three are located in medium-to-low density regions. The treatment of a diversified group provides insight into a wider variety of phenomena and enables the identification of of general trends transcending that diversity.

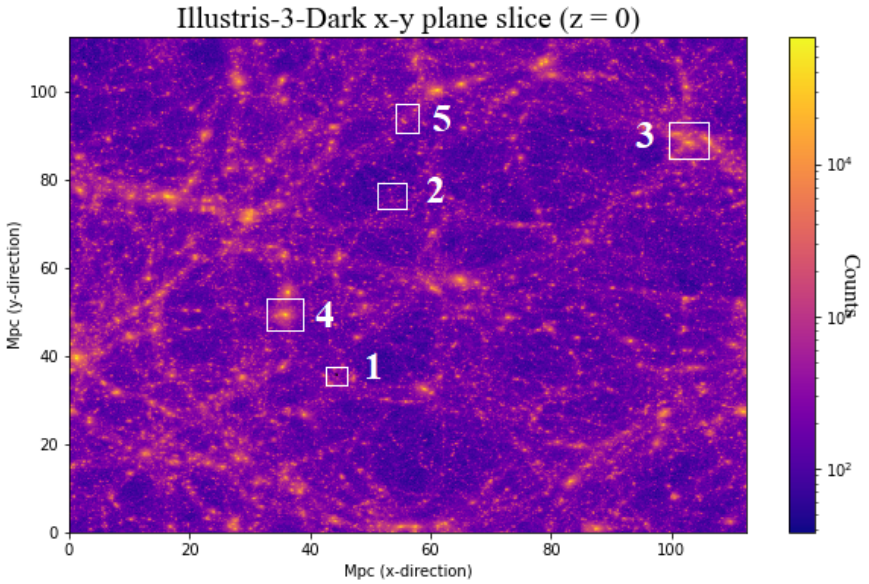

Figure 10: Location of the cluster environments selected for analysis. Two of them are massive, located in very dense regions, while the remaining three are smaller, with underdense surroundings.

The clusters were characterized by their corresponding dark matter subhalos, with their masses and radii, defined as the distance from the center enclosing half of the total mass, showed in table 1 below.

Cluster number	1	2	3	4	5
Mass $[10^{10} M_{\odot}/h]$	6.53	2.97	15.80	208.53	0.62
Radius [ckpc/h]	29.64	31.74	28.95	47.65	18.11

Table 1: The masses and radii of the dark matter subhalos in the investigated clusters. Cluster 1 is chosen as a case study. Note: the clusters might consist of multiple subhalos, so the true values are most likely higher, the table gives the best available estimate.

5.1 A case study of a single cluster

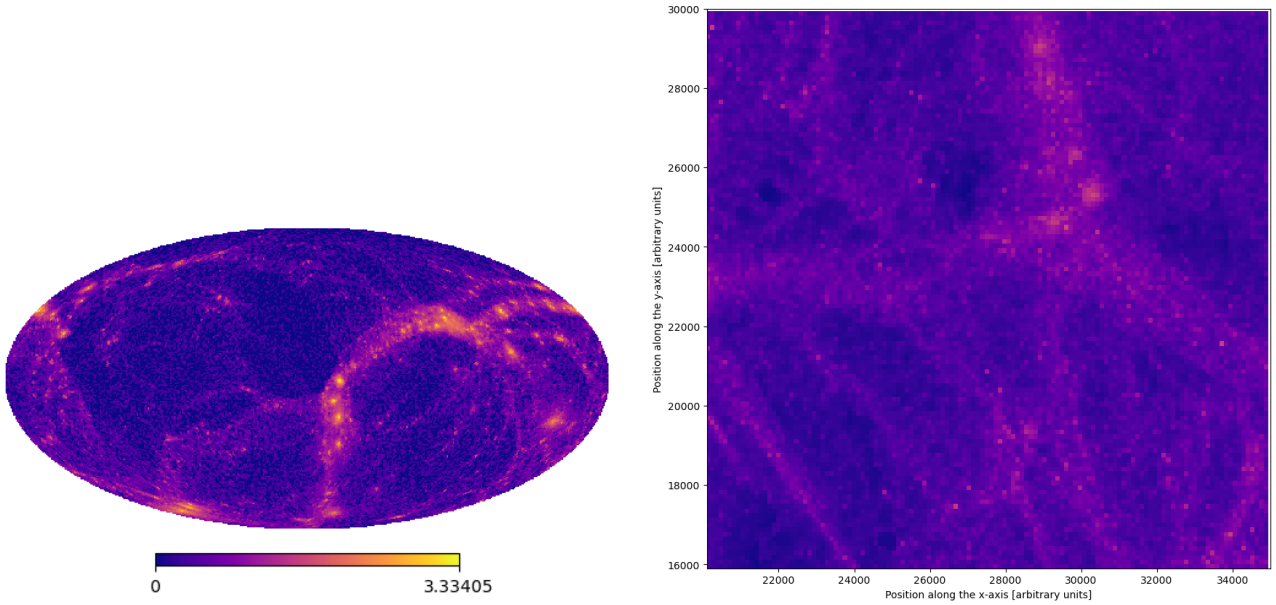

((a)) **((b))**

Figure 11: In (a), an example of a mass distribution map plotted from the perspective of a massive cluster, within a radius of 10 Mpc. Two filaments, a wall, and a void region can be distinguished within the skewed distribution. In (b), the Cartesian view of the cluster environment. The wall-like structure, as well as the attached filaments and voids, correspond to those in (a).

Figure 11 shows an example of a view on the Cosmic Web within a 10 Mpc radius from the perspective of a center of mass of a massive cluster, as well as the Cartesian view of the environment. Figure 11(a) illustrates an atlas of structures, where the majority of the mass appears to be focused on the eastern part of the sky. Two ”candidate” filament can be distinguished laying within an open, ring-like structure that could potentially be identified as a wall. The western region shows a large underdensity that could form a void.

Figure 11(b) provides additional context for the structure. The two large filaments on the right-hand side seem to be connected to the cluster at an angle, which is reflected by the filamentary hot spots laying close together in the projection, instead of being separated somewhat symmetrically, which would reflect a straight filament crossing through the cluster. Moreover, the overall density pattern resembles a wall-like structure towards the left of the cluster, however, a definite conclusion based on the Cartesian case could only be established upon examination of multiple slices.

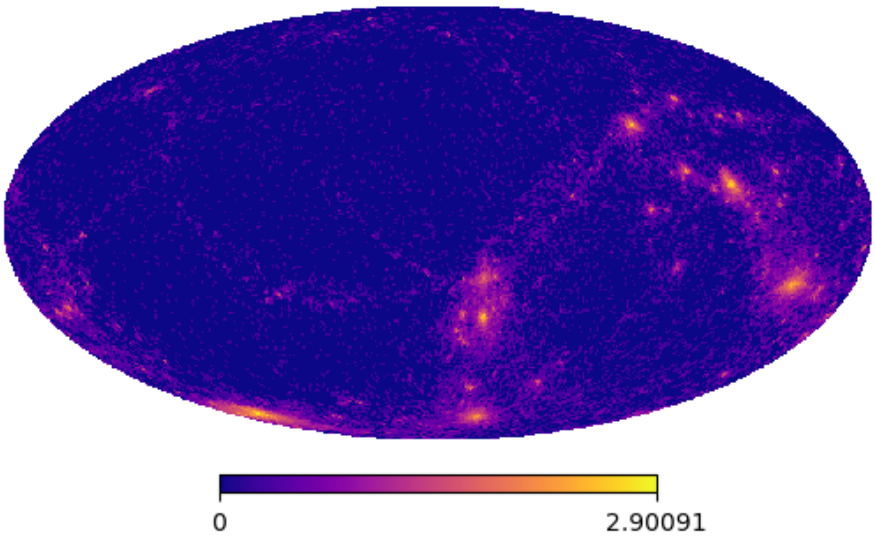

Figure 12: An example of a mass distribution map plotted from the perspective of a massive cluster, within a radius of 5 Mpc. The filaments can be distinguished from the walls.

In figure 12, the closer neighbourhood is examined within a 5 Mpc region and the dominating structure crystallizes. Around four filaments are seen as separate entities, instead of being a part of a wall, two of them being the fainter ones that could be identified in to the left of the cluster viewed in figure 11(b).

5.2 A comparative study of an array of diverse cluster environments

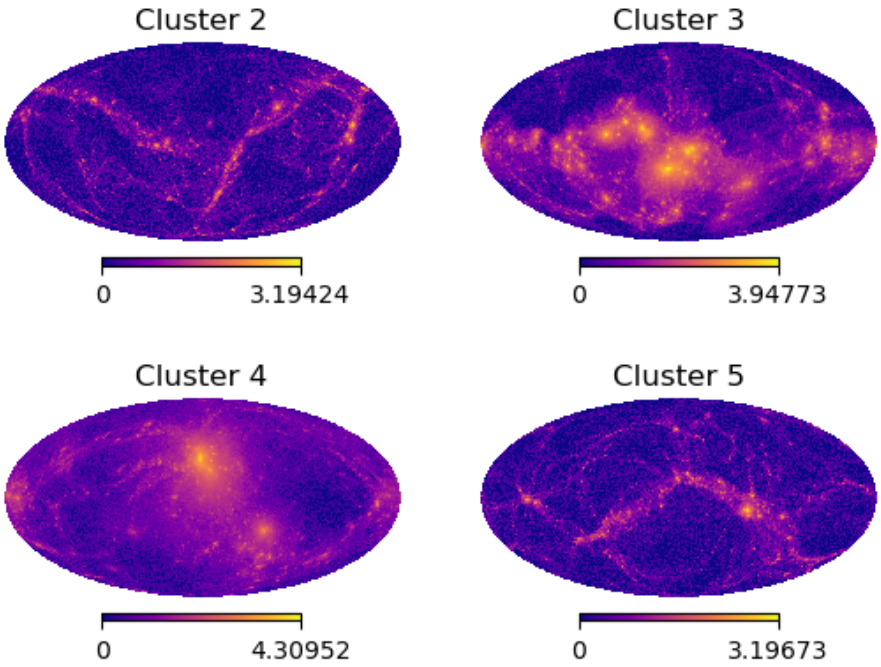

Figure 13: An atlas of maps showcasing the mass distribution within a 10 Mpc radius of four clusters: angular perspective.

The same procedure can be repeated for four more clusters, forming a total sample of 5, which are highlighted in figure 13 for the 10 Mpc regime. A diversity of environments found in the Cosmic Web is reflected. The smaller Clusters 2 and 5, with less pronounced surrounding structure, show smaller filaments and more distinct walls. Those sheets are visible with exceptional clarity in Cluster 2, where two full, crossed-over rings can be distinguished. Clusters 3 and 4, on the other hand, are more massive and dominated by large filaments, with weaker wall structure present.

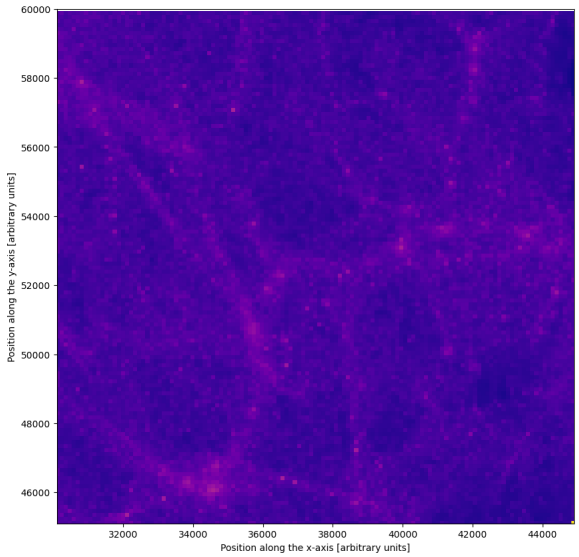

((**a**)) Cluster 2

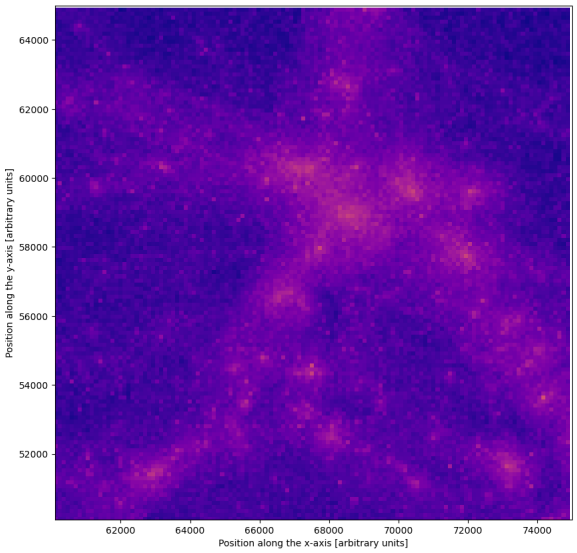

((**b**)) Cluster 3

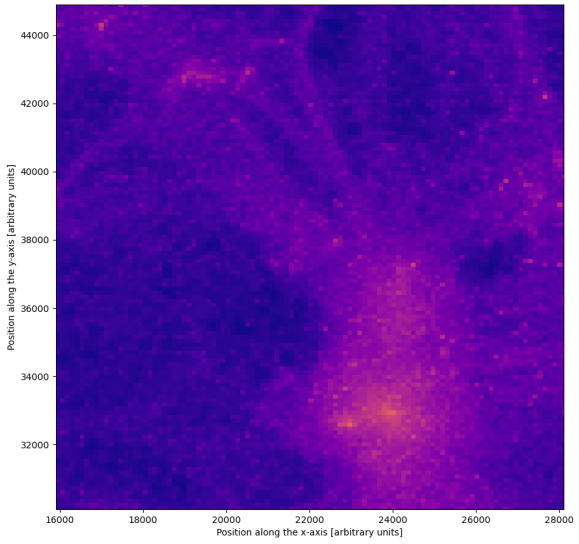

((**c**)) Cluster 4

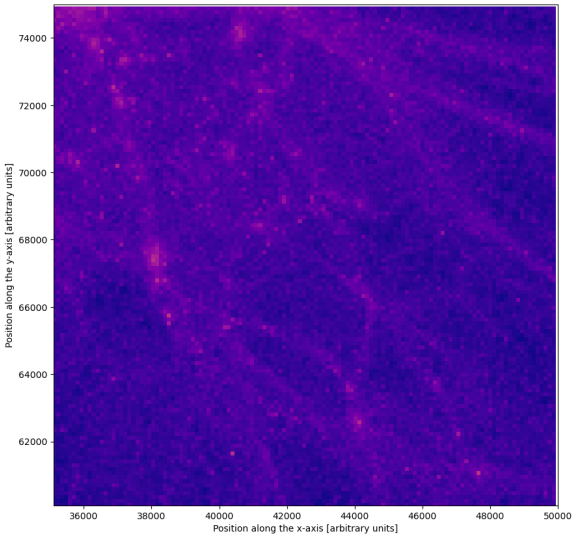

((**d**)) Cluster 5

Figure 14: An atlas of maps showcasing the mass distribution within a 22.5 Mpc-long box for four cluster environments: Cartesian perspective.

Additionally, figure 14 illustrates the wider environment in which the clusters are located. Clusters 2 and 5 are indeed less prominent in their neighbourhood, which is composed of multiple smaller filaments, suggesting that the ring-like structure might also be a disconnected filament located in close proximity to the cluster. Moreover, they also appear to be quite spherical in shape. Clusters 3 and 4, seemingly more elongated and containing more substructure, have very prominent, numerous filamentary structures in their surroundings. The also occupy a larger volume, meaning that the angular analysis within a given radius reflects, generally, the environment to a lesser extent than in the less massive case, introducing an intrinsic bias.

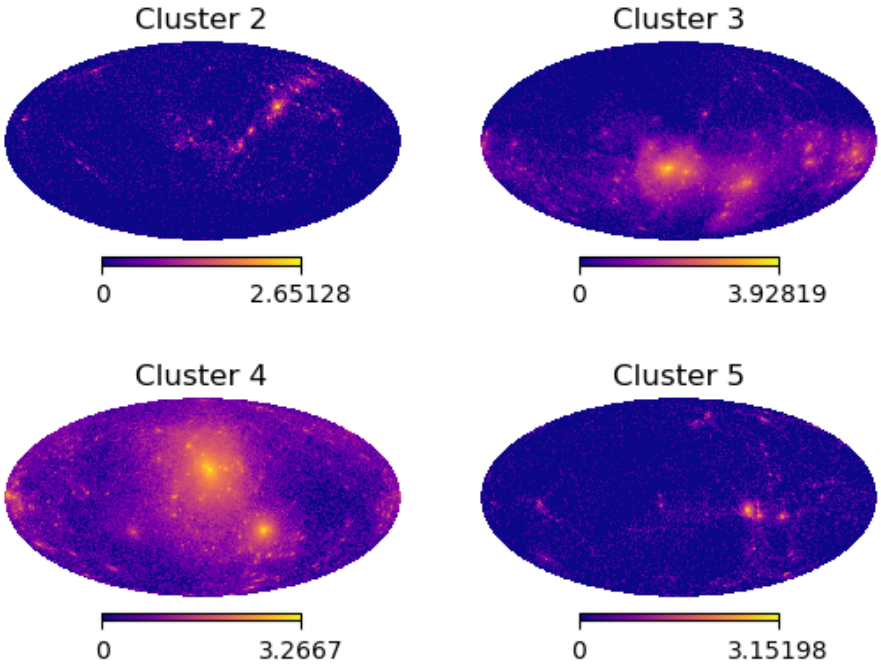

Figure 15: An atlas of mass distribution maps for four clusters within 5 Mpc radius.

Reducing the radius within which the structure is examined offers additional insight into the elements of neighbourhood composition which are otherwise overshadowed by their more dominant siblings. Figure 15 exemplifies this behaviour, especially in Cluster 2 and 5, as the connected filaments become visible, suggesting they dominate the environment on smaller scales. Clusters 3 and 4, too, loose the weak, wall-like features. Moreover, the all the selected regions show an asymmetry between the incoming filaments, meaning they rarely form a 180 degree angle with each other.

The tendency of more massive clusters to include more filaments in their neighborhood has been found before in studies by Aragón-Calvo et al [43], Colberg et al [44], and most recently by Codis et al [45], and ultimately has been baptised as the ”connectivity” of the Cosmic Web. The former paper includes the finding that the most massive clusters seem to have, on average, five connecting filaments, and less massive ones – around two. That is indeed the case for Clusters 2 and 5, which seems to contain two filaments, while Clusters 1 and 3, the most massive in the atlas, show up to four. Cluster 4 is somewhat more ambiguous, since it belongs to the more massive case, but upon inspection shows only two filaments. The seeming inconsistency could be explained by the very massive filaments rendering the smaller ones impossible to resolve. The cluster could also simply be an outlier, laying within a single, prominent filament.

Moreover, the heavier clusters include not only more, but also more massive filaments. The trend has been observed before as a correlation between the masses of the clusters and the connected filaments [46]. The findings appear to be consistent with such phenomenon, where the examined environments follow this tendency closely, for instance with the least massive Cluster 2 having the smallest filaments.

A correlation has also been established between the length of the filaments and their curliness, the latter defined as a ratio between the distance between the ends of the filaments and its length. It

was shown that shorter filaments tend to be less curly [47]. The more massive clusters are located in overall denser neighborhoods, meaning they lie in proximity to other clusters, presumably leading to the connecting filaments being shorter. The less massive ones, on the other hand, do not have a neighbour as close to them, implying the incoming filaments could be longer. As such, it is possible that such curl could lead to filaments appearing more elliptical in projections, which could be the case for Cluster 2.

6 Mass distribution around cluster nodes: spherical harmonic analysis

The spherical harmonic series defined in equation 6 and the corresponding coefficients were extracted based on the HEALPix map, serving as the basis for the analysis. The spherical harmonics were first plotted for each map in increasing degree of angular momentum and the corresponding a_ℓ^m coefficients, where $\ell = 1$ reflects the asymmetry between the two hemispheres, and the higher-order contributions reveal progressively intricate structures. Following the initial visualization, the mass distribution map is contrasted with a map showing the residue after subtracting the terms in ℓ up to 4 in its reconstruction, corresponding to the most spherical contributions, with the goal of investigating the filamentary and wall-like structures and substructures. Lastly, the maps are analysed based on their power spectrum in terms of C_ℓ coefficients. Such procedure was conducted for a total of five clusters, where one of them was selected as a case study and the remaining four were treated in a comparative framework.

6.1 A case study of a single cluster

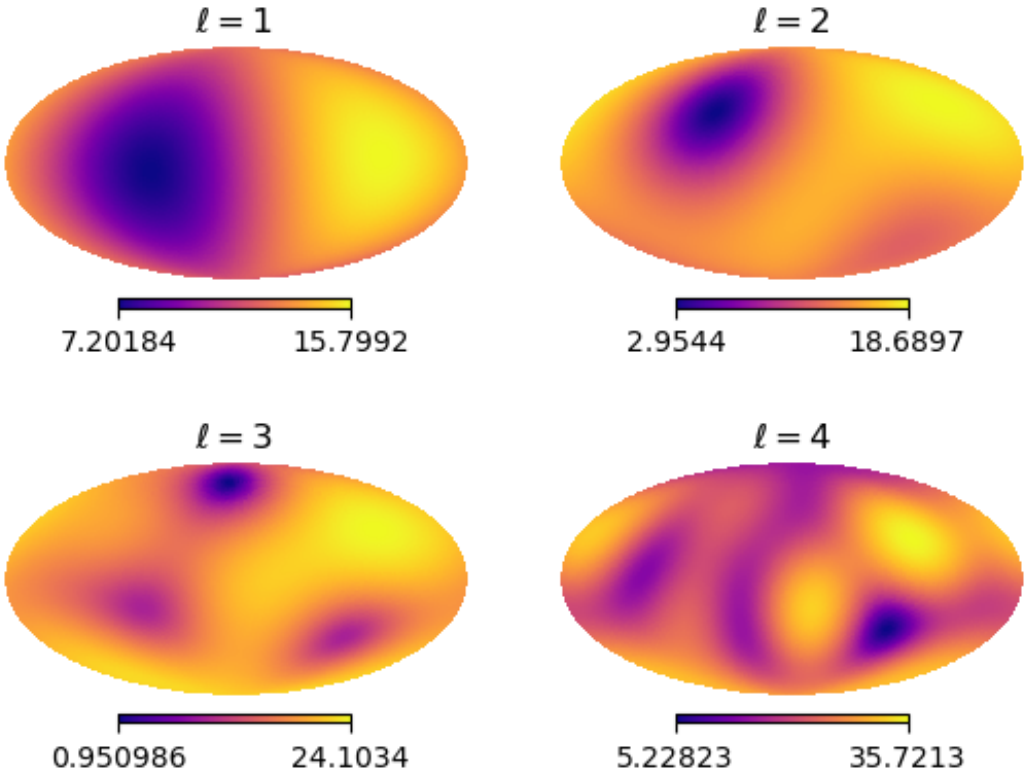

Figure 16: Reconstruction of a map of mass distribution around a cluster. Each next plot contains an additional term in higher angular momentum ℓ in the spherical harmonic series, revealing additional structures.

Figure 16 shows the reconstruction of the mass distribution plot in figure 11 with increasing angular momentum ℓ included in the expansion. The asymmetry between the left and right hemispheres is quantified in including the first-degree approximation and confirms the observations based on visual, qualitative analysis; the eastern hemisphere does indeed contain most of the mass. The second-degree

plot shows an echo of the void-like region identified beforehand, and the next values of angular momentum slowly start including the candidate filaments. The filamentary details and walls are not yet visible, hinting at the existence of significant substructure.

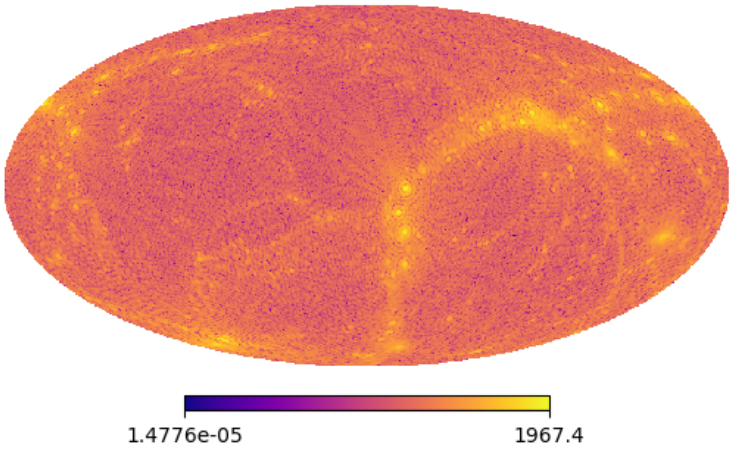

Figure 17: Reconstruction of the density map of the case study cluster (figure 11) approximated to angular momentum degree ℓ of 400

The reconstruction can be conducted for a large angular momentum, limited by computing time and the map resolution. An example of such high-ℓ setup can be seen in figure 17, where a sum of the first 400 values were included in the spherical harmonic series. Such exercise completes the picture of map reconstruction from its associated spherical harmonic coefficients. Including those higher-order terms facilitates the rise of a more detailed structure, where the complex, non-spherical elements surface. Comparing maps in figures 11 and 17 serves as a verification of the accuracy of the analysis, showing a convergence between the original and reconstructed maps as higher-order terms are included.

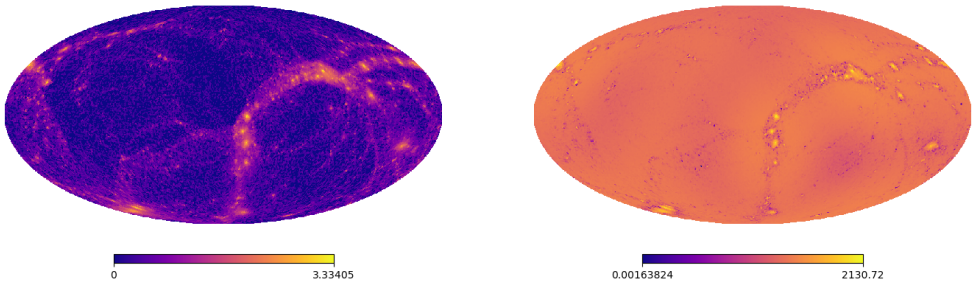

Figure 18: A comparison between the original density map (left) and its residue (right) after removing the elements belonging to the $\ell = 4$ regime.

Having obtained the coefficients in the spherical harmonic series, certain structures can be removed from the map through subtracting an approximation, such as the ones in figure 16, from an original distribution map. Figure 18 shows a comparison between the two when the first four terms in the spherical harmonic series are subtracted, effectively removing the more spherical structures. Hence, filaments and parts of the wall are highlighted on a largely uniform background as a result.

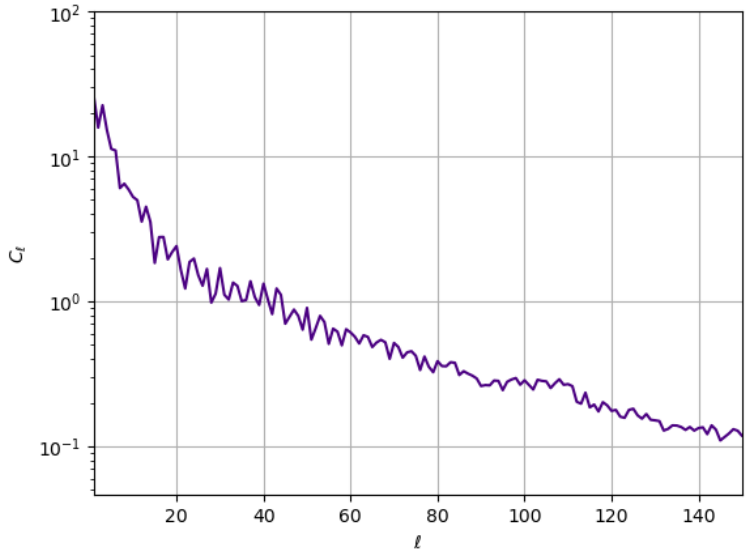

Figure 19: Power spectrum of the map in figure 11.

The data was also analyzed based on the map's associated power spectra, as highlighted in figure 19. The C_ℓ coefficients follow from equation 8 and allow for decomposing the signal into frequency-based components. The showcased spectrum shows a high initial peak which is followed by a steadily decreasing trend with increasing angular momentum. Such behaviour indicates the dominance of the underdense, spherical regions within the map, while the more intricate structure appears fainter. However, the contributions in high angular momentum components are not negligible, forming another proof for the presence of intricate substructure.

6.2 A comparative study of an array of diverse cluster environments

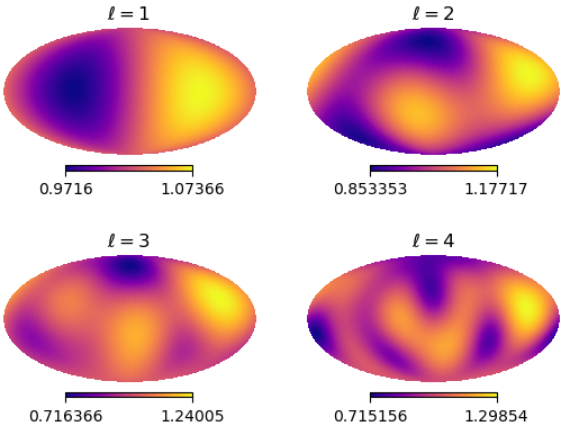

((**a**)) Cluster 2

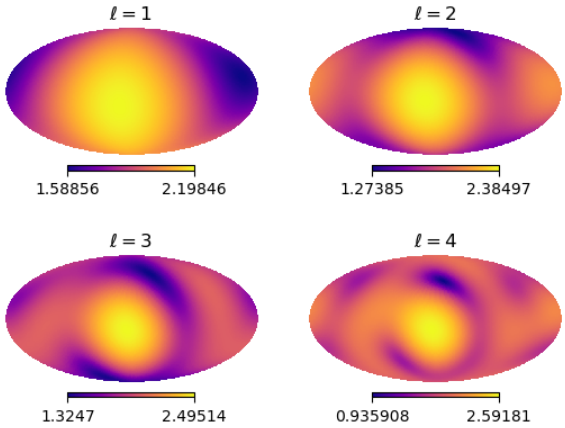

((**b**)) Cluster 3

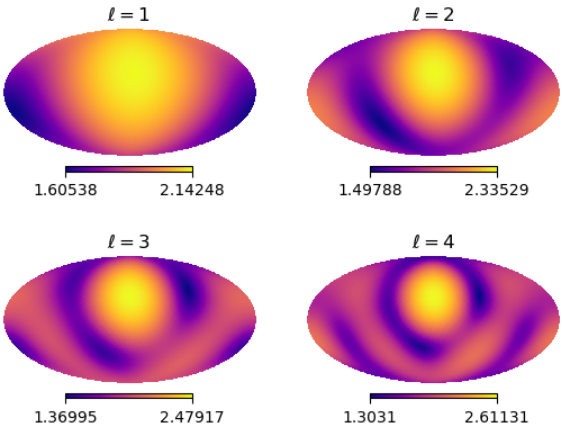

((**c**)) Cluster 4

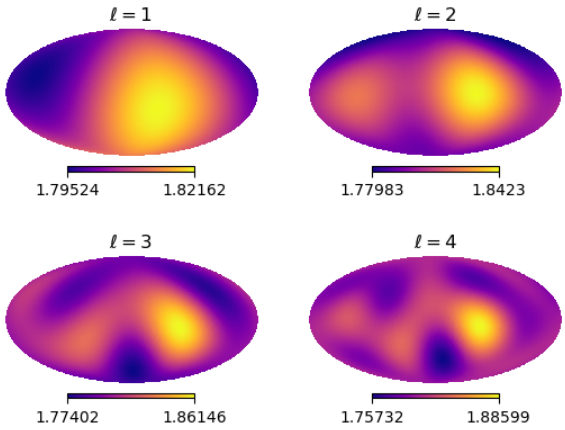

((**d**)) Cluster 5

Figure 20: Spherical harmonic reconstruction in increasing degrees of angular momentum ℓ for different clusters.

Figure 20 compares a spherical harmonic reconstruction in increasing order of angular momentum for four mass distribution maps of four clusters. Once again, the asymmetry is highlighted. Clusters 3 and 4 appear to be dominated by their massive filaments, which are central, bright, and emerge first, while Clusters 2 and 5 follow a pattern similar to the case study, where underdense regions seem dominant. The clusters with prominent filaments also contain more mass overall, suggesting that density is correlated with the dominant type of structure around the cluster, as highlighted in the visual examination.

Moreover, all clusters seem to start developing first hints of filamentary structure at $\ell = 2$, however, even with $\ell = 4$ it is not as defined as expected considering filaments to be within the quadrupole contribution, meaning the visually identified structures include notable substructure.

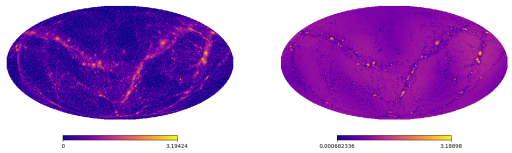

((**a**)) Cluster 2

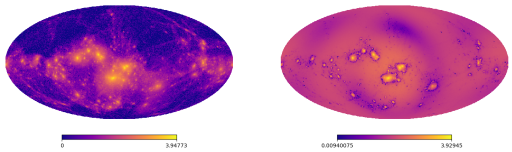

((**b**)) Cluster 3

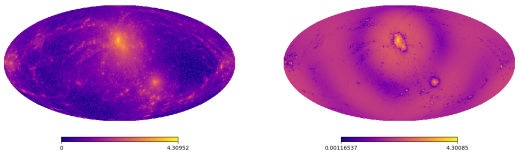

((**c**)) Cluster 4

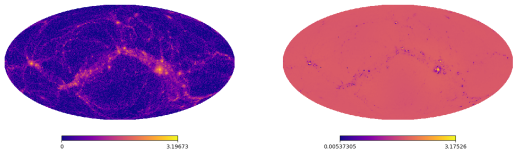

((**d**)) Cluster 5

Figure 21: A comparison between the original mass distribution map and the residue after subtracting contributions up to $\ell = 4$ for selected clusters.

Figure 21 offers insight into the nature of the structure around the clusters based on the map residue after subtracting the spherical structures. The filaments identified in Clusters 2 and 5 are seen embedded into a wall, while the ones belonging to Clusters 3 and 4 seem to not be a part of a larger structure. Such behaviour can be tied to the aforementioned bias; as the more massive clusters contain a slightly different type of environment, perhaps the walls are not visible on the given scale.

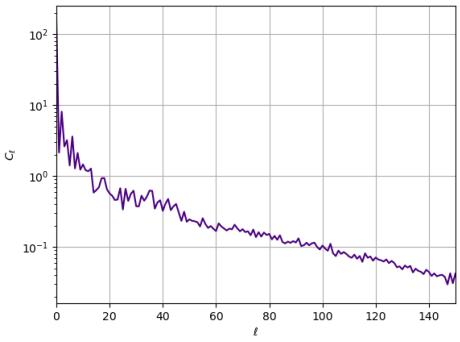

((a)) Cluster 2

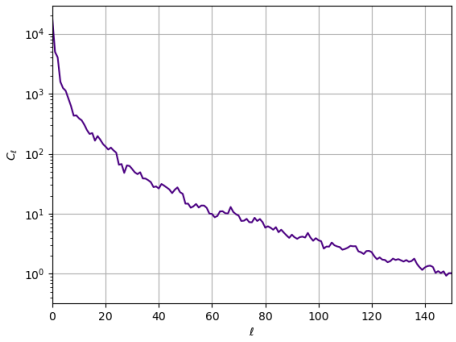

((b)) Cluster 3

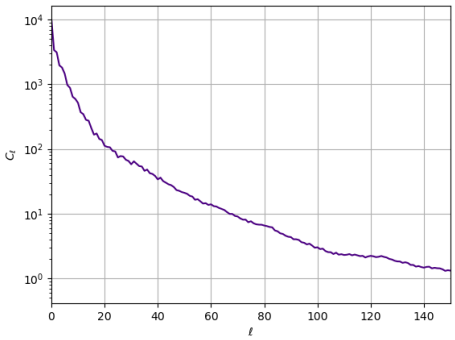

((c)) Cluster 4

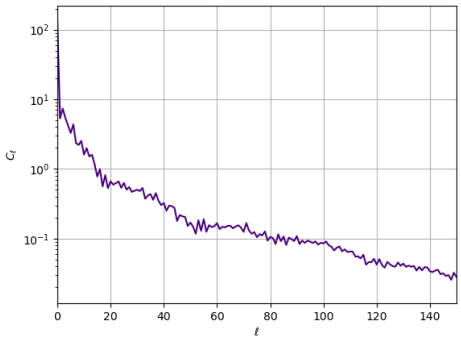

((d)) Cluster 5

Figure 22: Power spectra of selected clusters visualized as a function in C_ℓ.

Cluster number	1	2	3	4	5
Power law: *n* coefficient	-0.82	-0.68	-1.08	-0.93	-0.75

Table 2: The power law *n* coefficients of the spectra of the selected clusters, determined with a least-squares fit.

Table 2 summarizes the *n* coefficients of the power spectra of the maps included in figure 22. A tendency for less dense clusters, such as 2 and 5, to have a sharp peak around $\ell = 0$ and a rapid fall-off is revealed. Clusters 3 and 4, on the other hand, have spectra that decrease less rapidly, as indicated by a more negative *n* coefficient. Such behaviour can be explained by the former case including prominent voids, which are the most spherical elements of the Cosmic Web. The spectra in the latter case reflect the massive filaments, but also reveal, yet again, a strong substructure.

The substructure of the Cosmic Web is present in all its elements and its existence can be interpreted as evidence for the hierarchical development of the large-scale structure [48], [25]. Hence, the slower-diminishing power spectra of Clusters 3 and 4 also hint at the possibility that those clusters having formed earlier, with more time for development of additional layers of substructure.

7 Mass flow around cluster nodes

Investigating the mass migration was chosen as a complementary tool to the mass distribution study of the angular view of the Cosmic Web. The nature of contributions from different elements of the structure reveal their formation history. Moreover, the direction of the cosmic flow can be used as a classification aid applied to different elements of Universe's anatomy, as was showcased by the characteristic velocity fields. As such, the two views, of mass distribution and flux, form a uniform picture united by the themes of connectivity, and, as is revealed by the following investigation, hierarchy.

The flux and the mass distributions are intimately related through the Gauss law given in equation 9, which indicates that the total flux is the integral of the radial velocity field over the surface area, in this case a sphere of a given radius around a cluster [40].

$$\Phi \equiv \int_S \mathbf{v} \cdot \hat{\mathbf{n}} \cdot d\mathbf{a} \tag{9}$$

Here $\hat{\mathbf{n}}$ is a vector normal to the surface. Flux Φ can also be expressed as a product of the radial component of the velocity field with the associated mass density. The correlation between the two underlines the need for including influx in the picture of cluster environments, their morphology and their dynamics.

The flow of mass within the environment was studied by an alternative method, based on the mass distribution maps, which eliminated the need for approximations and numerical solutions to equation 9. The flux was calculated by comparing the mass in each pixel between different redshifts, separated by $z = 1$, between $z = 0$ and $z = 5$. The procedure was done by simple subtraction of the older histogram from the more recent one, outcome of which was again plotted in Mollweide projection for the sake of visually identifying the contributing regions.

Flux was also visualised in Cartesian view, through plotting the velocity field on top of the mass distribution obtained through DTFE. The resulting maps show a global perspective on mass migration, complementing the findings in angular analysis.

The comparison of flux contributions from different Cosmic Web elements required discerning their regions in the map. The original mass distribution plot was masked for different values and evaluated visually for whether the remaining pixels showed the desired structure. The same masking was applied to the flux maps in order to keep the investigated region consistent, and the mass difference in the remaining pixels was averaged, which allowed for a direct comparison between the different elements.

7.1 Visual evaluation

The mass flow was inferred based on the difference between mass distribution maps at different redshifts. The flux investigation focuses on the most recent changes by comparing the densities at redshifts $z = 0$ and $z = 1$. A comprehensive overview of the evolution between redshifts $z = 0$ and $z = 5$ can be found in the Atlas attached in the Appendix A, where trends coherent with the investigated case are shown.

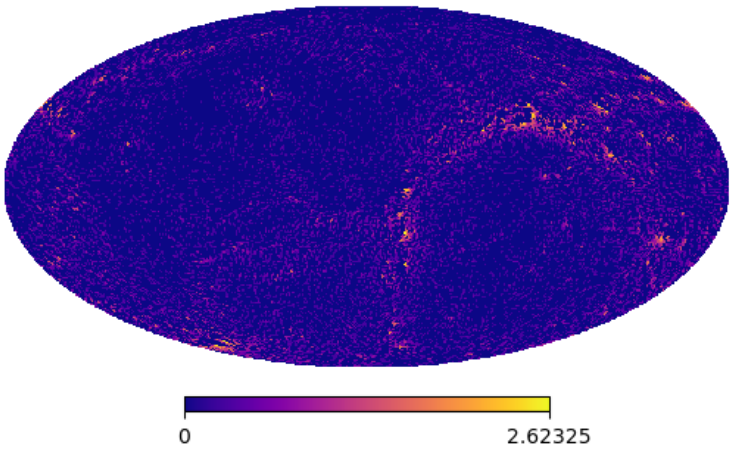

Figure 23: Mass inflow in the case study cluster within a radius of 10 Mpc.

Figure 23 illustrates the inflow of mass within the cluster examined as a case study. The flux is located predominantly in areas where the filaments were located through spherical harmonic analysis (see figure 18 for comparison), with minor contribution from the wall-like structure. The rest of the map shows almost no inflow.

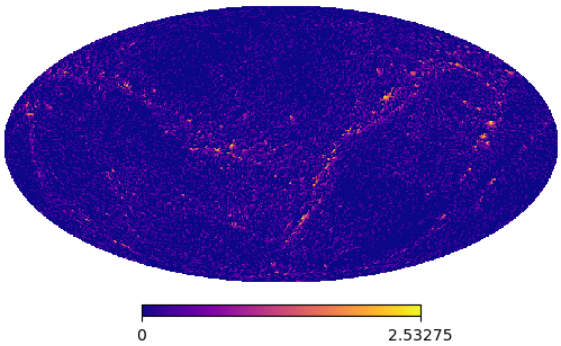

((**a**)) Cluster 2

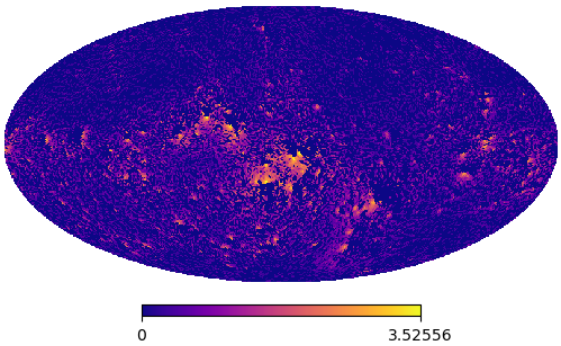

((**b**)) Cluster 3

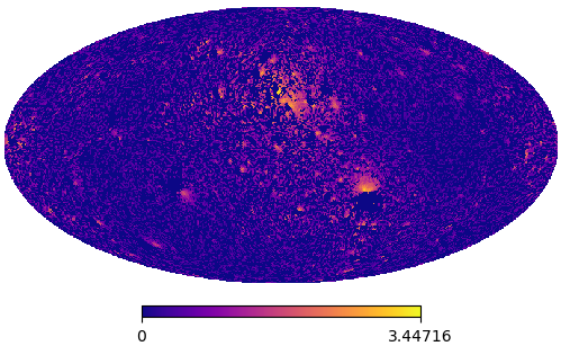

((**c**)) Cluster 4

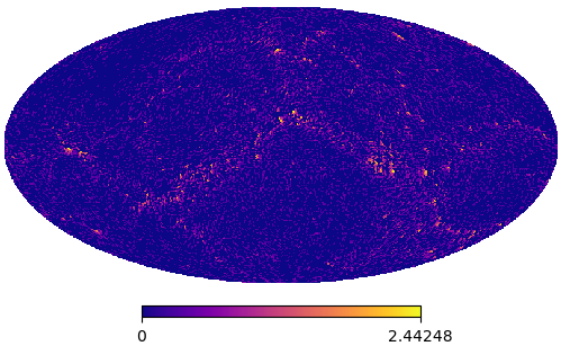

((**d**)) Cluster 5

Figure 24: Mass inflow in various clusters within a radius of 10 Mpc.

The mass flow consideration extends to a variety of cluster environments, as illustrated in figure 24.

The more massive Clusters 3 and 4 show a much higher overall flux through the filaments, while Clusters 2 and 5 are fed by a combination of the walls and small filaments.

Overall, the radial component of the velocity field corresponds well with the mass distribution around clusters. Such behaviour was already observed by Villumsen and Davis [7], who investigated the mass inflow to the a number of clusters through spherical analysis and concluded that the force and velocity fields show exceptional alignment.

7.2 Contributions from filaments and voids

Following the visual investigation of mass flow into the cluster, the contributions from the voids and the clusters were separated at various redshifts up to $z = 5$. The two can be discerned by the means of visual investigation of Cartesian mass distribution plots with the associated velocities plotted on top, obtained using DTFE, and quantitatively, by studying the mean influx in the areas identified as filaments and voids plotted as a function of redshift in the angular regime.

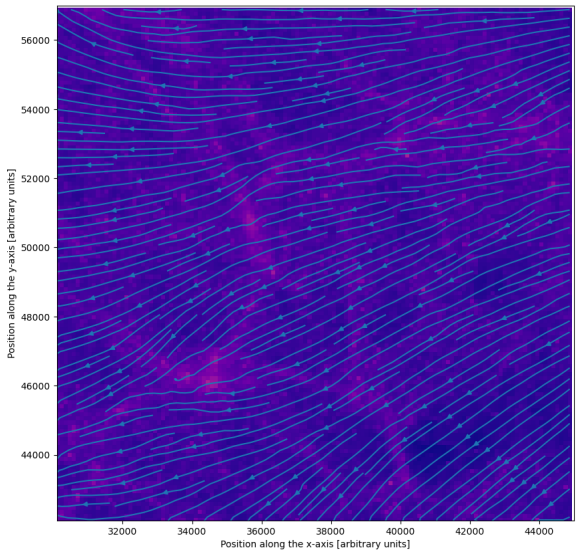

((**a**)) Cluster 2

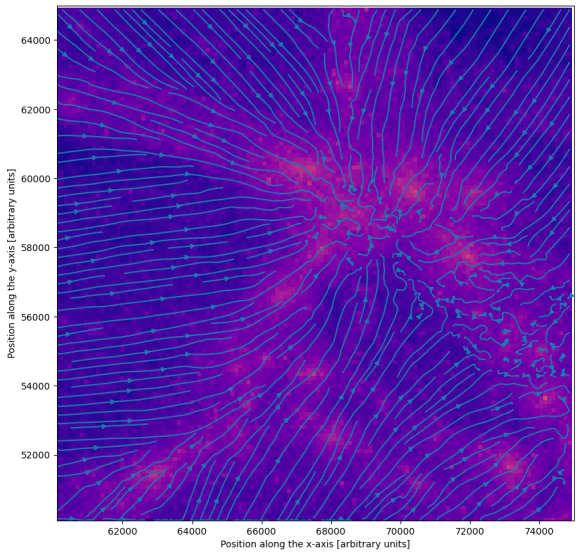

((**b**)) Cluster 3

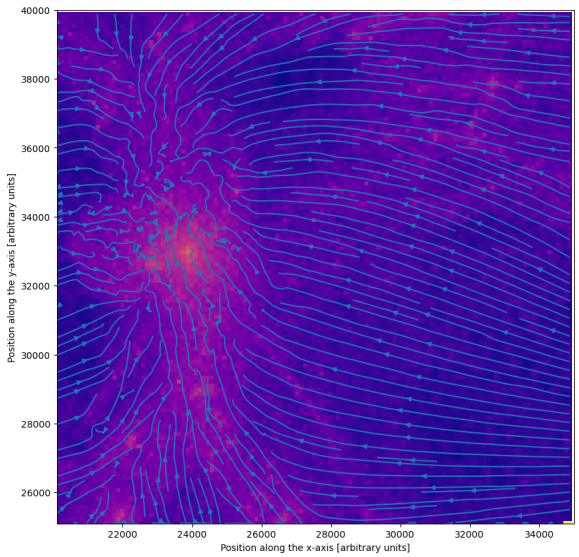

((**c**)) Cluster 4

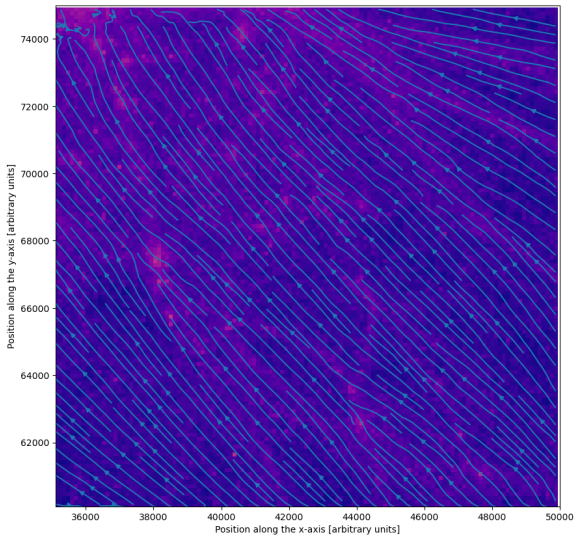

((**d**)) Cluster 5

Figure 25: Mass migration around an atlas of clusters illustrated by the velocity associated with the mass distribution.

Figure 25 shows the velocity field plotted alongside the density distribution showed from the Cartesian perspective, implemented with DTFE. A pattern emerges, where the massive clusters show a clear accretion of mass from the surrounding structures, while the smaller ones seem to be completely dominated by sheer, hinting at the overall low density of the region. In the former case, the voids appear to be losing their mass both through filaments and directly to the cluster, while the filaments provide inflow to the cluster exclusively.

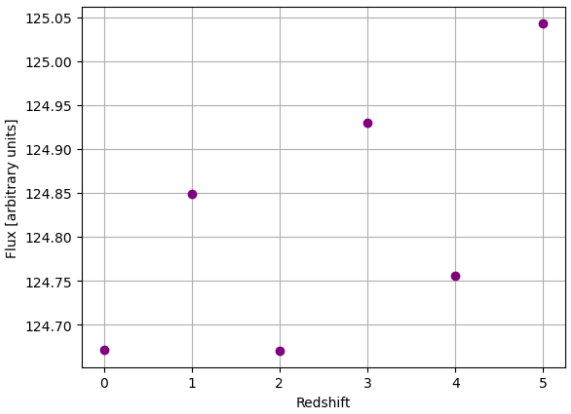

((a)) Void contribution to the mass inflow

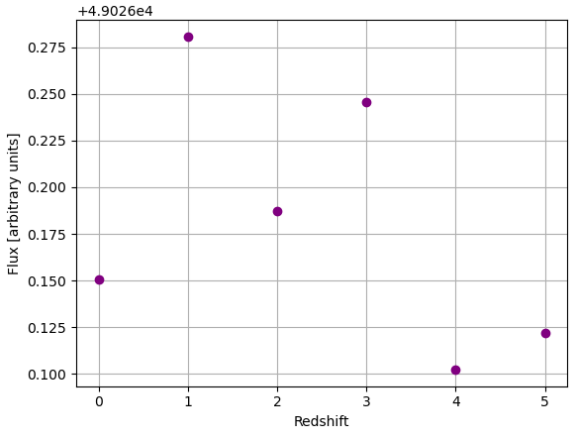

((b)) Filament contribution to the mass inflow

Figure 26: Comparison between the mass inflow from the voids and the filaments within Cluster 1.

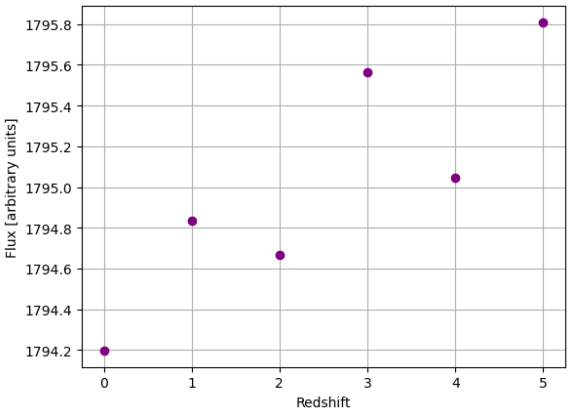

((a)) Void contribution to the mass inflow

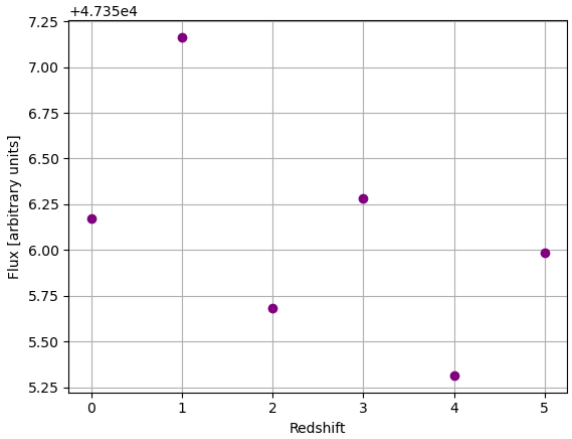

((b)) Filament contribution to the mass inflow

Figure 27: Comparison between the mass inflow from the voids and the filaments within Cluster 3.

In the angular framework, detangling the two contributions seems to reveal their opposite behaviours, as seen in figure 27. The inflow from the voids diminishes at smaller redshifts, suggesting the decreasing relevance of mass influx from those regions. On the other hand, filaments provide an increasingly high flux with decreasing redshifts. The same pattern is observed for all five clusters, which is extensively illustrated in the Appendix B. Moreover, the magnitude of flux due to filaments is roughly two orders of magnitude higher than that from the voids, despite the much larger volume they occupy.

The diminishing void contribution can be explained by the merging of the voids due to the tidal force field. In the growth process their potential also becomes deeper [26]. Moreover, their substructure is lost in mergers, contributing to the overall decrease in density [49]. However, ultimately, density alone is not a sufficient classification criteria, as the different Cosmic Web elements have largely overlapping characteristic densities. In the case of comparing filaments and voids, such choice can be justified by the large overall difference in their profiles, but when comparing the inflow contributions one has to be aware of the bias introduced by the selected sampling method [43].

Considering the order of the flow outlined by the principles of gravitational instability and the tidal forces such behaviour seems justified. The incoming mass is sourced mostly from the filament, while the mass from the walls contributes slightly, but most of its outflow is likely towards the filament instead of the cluster. The void regions seem to have a significantly smaller contribution, most probably losing their mass to the walls, instead of in the radial direction towards the cluster.

Moreover, spherical analysis of cluster inflow has previously showed to underestimate its magnitude for denser clusters [7]. Such behaviour is exhibited in the clusters under investigation here, which seem to show an inflow of roughly the same order of magnitude for all cases, while the less massive ones located in underdense environments would be expected to have a somewhat smaller influx.

8 Summary of main contributions

The Cosmic Web, the largest-scale, foam-like structure composed of clusters, filaments, walls, and voids, was examined with a focus on clusters and their environment. The analysis was done twofold: in a holistic way, combining qualitative and quantitative view from the perspective of five massive clusters within two different radii of 5 and 10 Mpc, and based on visual assessment of a Cartesian view of the wider regions. The former was made possible by taking an angular approach to the problem, which highlighted the connectivity of the structure and its hierarchical nature, while facilitating an in-depth analysis through detangling the environment into frequency-based components. Through the ease of identification of different elements of the Cosmic Web, the approach also enabled the analysis of the mass inflow on a component-by-component basis, inspired by Villumsen and Davis [7].

The Illustris-3-Dark dataset provided a basis on which the investigation was conducted. HEALPix complemented the simulated data as the main framework for analysis, a choice motivated by its high-resolution of sphere pixelation and versatile spherical harmonic analysis functions. The pixels were treated as histogram bins for the Illustris particles, creating a mass distribution map. Spherical harmonic analysis was employed to extract information from said maps, through reconstruction in increasing degree of spherical harmonics, residues after subtracting spherical structures, and analysing the power spectrum. DTFE served as a qualitative aid in the investigation, illustrating the density and velocity fields of selected environments.

The clusters were selected to represent a variety of environments and surrounding structures. The arising patterns could be sorted into two broad categories of more and less massive clusters. The more massive ones showed more pronounced, larger, and more numerous filaments outshining the walls, while the other group presented defined walls within which other structures resides, with two attached filaments on average. Such behaviour was concluded based on the mass distribution comparison between the plots at different radii and the prominence of features with spherical harmonic reconstruction. The findings were deemed to be in agreement with previous studies, where cluster mass was correlated with the number and mass of attached filaments. Moreover, based on the power spectra it was also observed that the more massive clusters show more elaborate substructure. It is suspected that those structures could have started developing earlier, allowing them a longer time to create the additional structural layers.

The analysis of the mass flow around the selected clusters, both through angular approach and examining the velocity field, revealed that filaments have the highest contribution, in accordance with the gravitational instability theory and implications based on tidal forces. The voids' influence proved to be, on average, two orders of magnitude smaller. Moreover, by comparing the flux at different redshifts it was concluded that the filamentary contribution is increasing with time, while voidal one diminishes. The behaviour was obeyed by all clusters regardless of whether they were dominated by the local velocity flows or the cosmic sheer. This finding was connected to the merging nature of void evolution, which leads to erasure of substructure and hence, lowers the overall density of the regions.

The findings obtained include an intrinsic bias which arises due to the nature of the selected clusters and the method of distinguishing between the elements of the Cosmic Web. Since the more massive clusters span over a bigger volume, the examined radii cover a slightly different extent of the enviroment than in the less massive case. In future work, it would be beneficial to investigate a larger

variety of radii to encapsulate the fullest view of the cluster regions. Moreover, when investigating the flux, the filaments and voids were discerned based on density criteria, which has been found to be generally insufficient as a tool due to overlapping characteristics between different elements. The choice here was motivated by the large difference between the filaments and the voids, however, it would be beneficial to include a more sophisticated approach, such as implementing an external feature-identification algorithm, for instance NEXUS.

Overall, the angular approach taken in the investigation has proved itself to be a highly versatile tool. It allowed the study of connectivity, mass distribution and migration with a unique perspective, unavailable in Cartesian analysis. Comparing the HEALPix mass distribution maps with the Cartesian DTFE counterparts reveals that the structure of the Cosmic Web is easier to discern in the former case, offering a more detailed view.

9 Conclusion

The angular perspective that was the spine of the study proved to be an excellent, versatile tool. The insight into the connectivity and complexity of the structure could be formed both on visual and spherical harmonic ground. Together with DTFE's effectiveness in discerning the intricate structure, the two paint a coherent picture of the mass distribution and flow within the large-scale structure.

Based on visual and spherical harmonic analysis clusters were separated into the general categories of more and less massive ones. The more massive cluster environments, such as those of Clusters 3 and 4, were found to contain more substructure as observed in their spherical harmonic reconstruction and power spectra. They were also dominated by numerous filaments, as opposed to the walls prominent in the less massive environments, which was inferred by the type of structure crystallizing at lower angular momentum coefficient values. The findings are in agreement with preceding studies which showed a correlation between cluster mass and the number of connected filaments.

The mass flow was found to be dominated largely by the filaments, with other elements having a marginal contribution. The contribution of filaments appeared to become larger over time, while voids showed a diminishing trend. The phenomenon was ascribed to voids merging and becoming less dense over time, which renders them unable to provide a steady influx of matter despite their domination by volume. The trend was observed for all clusters, regardless of whether their environment was dominated by cosmic sheer or local velocity fields.

It is exceptional that there are general trends followed by all clusters despite the different environments they are located it. Differences such as the influence of cosmic sheer, the overall density, and the nature of the surrounding structure, do not diminish the general trends in mass migration. Simultaneously, the matter distribution is shaped by tidal forces and gravitational instability into a wide array of morphological wonders. Different environments facilitate differences between the structures dominating on given scales, and between the number of attached filamentsl

9.1 Outlook

The proposed study provides a general overview of the dynamics in cluster environments and serves as a point of departure for further investigation. In future work, the following ideas would be a natural extension, in somewhat increasing order of complexity.

The power spectrum analysis could be conducted for voids and filaments separately, based on the implemented density criteria. Such treatment would open the doors to a more accurate cosmic parameter determination, as those elements offer a view of a spectrum containing less interaction between different modes [6].

Moreover, the power spectra extracted from the mass distribution plots offer a starting point for determining cosmological parameters, however, they should be complemented by computing the bispectra as well. Biscpectral analysis would be the first of the higher-order statistical tools to turn to, while being the lowest order tool that offers insight into the shape of the structures involved [50]. As such, bispectra include terms relevant to improving the contraints of cosmological parameters [6].

Another intriguing avenue to follow is investigating the assembly time, or "age", of clusters through

spherical harmonic analysis. Comparing the mass distribution plots and their reconstructions using spherical harmonics of degree up to $\ell = 4$, which should include the first hints at filaments, could be used as a mean of determining the assembly time. Such study requires examining redshifts higher than $z = 5$, however, it would prove an insightful tool of constraining cosmological parameters of the early Universe [51]. Moreover, it would allow forming a definite answer to the question of whether among the selected clusters the more massive ones formed faster.

The feature identification used to determine the flux contributions from filaments and voids could be carried out using a classification tool such as NEXUS [52]. The method would be an improvement upon the basic segregation based on density, which suffers from the inherent problem of overlapping feature characteristics [43]. Moreover, the environments could be studied at an extended range of redshifts, increasing the statistical relevance of the findings.

Lastly, HEALPix histograms were used as a mean of determining mass distribution based on particle data from the Illustris-3-Dark simulation. The same method could be used by examining a point distribution provided by the DTFE algorithm. However, in the case of taking the clusters' perspective, it would need to be implemented in spherical coordinates – a task much more complicated than the Cartesian case, where space-filling, regular tilling is easier to achieve. Developing the algorithm for a different coordinate system would allow more accurate filament identification and flow classification thanks to its volume-weighing properties.

Bibliography

[1] Y. B. Zeldovich, "The theory of the large scale structure of the universe," *Symposium - International Astronomical Union*, vol. 79, p. 409–421, 1978.

[2] J. R. Bond, L. Kofman, and D. Pogosyan, "How filaments of galaxies are woven into the cosmic web," , vol. 380, pp. 603–606, Apr. 1996.

[3] V. Springel, C. S. Frenk, and S. D. M. White, "The large-scale structure of the universe," *Nature*, vol. 440, pp. 1137–1144, Apr 2006.

[4] M. I. Scrimgeour *et al.*, "The wigglez dark energy survey: the transition to large-scale cosmic homogeneity: Cosmic homogeneity in the wigglez survey," *Monthly Notices of the Royal Astronomical Society*, vol. 425, p. 116–134, July 2012.

[5] A. L. Coil, *The Large-Scale Structure of the Universe*, p. 387–421. Springer Netherlands, 2013.

[6] T. Bonnaire, N. Aghanim, J. Kuruvilla, and A. Decelle, "Cosmology with cosmic web environments-i. real-space power spectra," *Astronomy & Astrophysics*, vol. 661, p. A146, 2022.

[7] J. V. Villumsen and M. Davis, "Velocity Fields around Rich Clusters of Galaxies," , vol. 308, p. 499, Sept. 1986.

[8] M. E. Brown and E. J. Groth, "The shane wirtanen counts - observability of the galaxy correlation function," *The Astrophysical Journal*, vol. 338, p. 605, Mar 1989.

[9] M. Seldner, B. Siebers, E. J. Groth, and P. J. E. Peebles, "New reduction of the Lick catalog of galaxies.," , vol. 82, pp. 249–256, Apr. 1977.

[10] P. J. E. Peebles and E. J. Groth, "Statistical analysis of catalogs of extragalactic objects. V. Three-point correlation function for the galaxy distribution in the Zwicky catalog.," , vol. 196, pp. 1–11, Feb. 1975.

[11] A. Webster, "The clustering of quasars from an objective-prism survey," *Monthly Notices of the Royal Astronomical Society*, vol. 199, p. 683–705, Jul 1982.

[12] M. R. Blanton *et al.*, "Sloan Digital Sky Survey IV: Mapping the Milky Way, Nearby Galaxies, and the Distant Universe," , vol. 154, p. 28, July 2017.

[13] C.-A. Faucher-Giguere, A. Lidz, and L. Hernquist, "Numerical simulations unravel the cosmic web," *Science*, vol. 319, p. 52–55, Jan. 2008.

[14] M. Levi, C. Bebek, T. Beers, R. Blum, R. Cahn, D. Eisenstein, B. Flaugher, K. Honscheid, R. Kron, O. Lahav, P. McDonald, N. Roe, D. Schlegel, and representing the DESI collaboration, "The desi experiment, a whitepaper for snowmass 2013," 2013.

[15] E. Conover, "The largest 3-d map of the universe reveals hints of dark energy's secrets," Apr 2024.

[16] A. C. Rodríguez, T. Kacprzak, A. Lucchi, A. Amara, R. Sgier, J. Fluri, T. Hofmann, and A. Réfrégier, "Fast cosmic web simulations with generative adversarial networks," *Computational Astrophysics and Cosmology*, vol. 5, p. 4, Nov 2018.

[17] D. Nelson, A. Pillepich, S. Genel, M. Vogelsberger, V. Springel, P. Torrey, V. Rodriguez-Gomez, D. Sijacki, G. F. Snyder, B. Griffen, *et al.*, "The illustris simulation: Public data release," *Astronomy and Computing*, vol. 13, pp. 12–37, 2015.

[18] J. R. Bond, L. Kofman, and D. Pogosyan, "How filaments of galaxies are woven into the cosmic web," *Nature*, vol. 380, pp. 603–606, Apr 1996.

[19] N. I. Libeskind, R. van de Weygaert, M. Cautun, B. Falck, E. Tempel, T. Abel, M. Alpaslan, M. A. Aragón-Calvo, J. E. Forero-Romero, R. Gonzalez, S. Gottlöber, O. Hahn, W. A. Hellwing, Y. Hoffman, B. J. T. Jones, F. Kitaura, A. Knebe, S. Manti, M. Neyrinck, S. E. Nuza, N. Padilla, E. Platen, N. Ramachandra, A. Robotham, E. Saar, S. Shandarin, M. Steinmetz, R. S. Stoica, T. Sousbie, and G. Yepes, "Tracing the cosmic web," *Monthly Notices of the Royal Astronomical Society*, vol. 473, pp. 1195–1217, 08 2017.

[20] M. Gramann, M. Einasto, P. Heinämäki, P. Teerikorpi, E. Saar, P. Nurmi, and J. Einasto, "Characteristic density contrasts in the evolution of superclusters. the case of a2142 supercluster," *Astronomy & Astrophysics*, vol. 581, p. A135, 2015.

[21] V. G. Gurzadyan and V. M. Fimin, N. N. aand Chechetkin, "On the origin of cosmic web," *The European Physical Journal Plus*, vol. 137, Jan. 2022.

[22] E. Aurell, D. Fanelli, S. Gurbatov, and A. Moshkov, "The inner structure of zeldovich pancakes," *Physica D: Nonlinear Phenomena*, vol. 186, p. 171–184, Dec. 2003.

[23] Y. B. Zel'dovich, "Gravitational instability: An approximate theory for large density perturbations.," , vol. 5, pp. 84–89, Mar. 1970.

[24] S. F. Shandarin and Y. B. Zeldovich, "The large-scale structure of the universe: Turbulence, intermittency, structures in a self-gravitating medium," *Rev. Mod. Phys.*, vol. 61, pp. 185–220, Apr 1989.

[25] M. Cautun, R. van de Weygaert, B. J. T. Jones, and C. S. Frenk, "Evolution of the cosmic web," *Monthly Notices of the Royal Astronomical Society*, vol. 441, pp. 2923–2973, 05 2014.

[26] E. Platen, R. Van De Weygaert, and B. J. T. Jones, "Alignment of voids in the cosmic web," *Monthly Notices of the Royal Astronomical Society*, vol. 387, pp. 128–136, 05 2008.

[27] M. Cautun, R. van de Weygaert, B. J. T. Jones, and C. S. Frenk, "Understanding the cosmic web," *Proceedings of the International Astronomical Union*, vol. 11, p. 47–56, June 2014.

[28] M. Vogelsberger, S. Genel, V. Springel, P. Torrey, D. Sijacki, D. Xu, G. Snyder, D. Nelson, and L. Hernquist, "Introducing the Illustris Project: simulating the coevolution of dark and visible matter in the Universe," *Monthly Notices of the Royal Astronomical Society*, vol. 444, pp. 1518–1547, 08 2014.

[29] V. Springel, "E pur si muove:galilean-invariant cosmological hydrodynamical simulations on a moving mesh," *Monthly Notices of the Royal Astronomical Society*, vol. 401, p. 791–851, Jan. 2010.

[30] R. van de Weygaert and W. Schaap, *The Cosmic Web: Geometric Analysis*, p. 291–413. Springer Berlin Heidelberg, 2008.

[31] W. E. Schaap and R. van de Weygaert, "Continuous fields and discrete samples: Reconstruction through delaunay tessellations," 2000.

[32] R. W. Shores and E. J. Wegman, "Bounds on delaunay tessellations," *Wiley Interdisciplinary Reviews: Computational Statistics*, vol. 2, no. 5, pp. 571–580, 2010.

[33] D. Phillips, "Tessellation," *Wiley Interdisciplinary Reviews: Computational Statistics*, vol. 6, pp. 202–209, 5 2014.

[34] J. Blazek, "Chapter 11 - principles of grid generation," in *Computational Fluid Dynamics: Principles and Applications (Second Edition)* (J. Blazek, ed.), pp. 373–413, Oxford: Elsevier Science, second edition ed., 2005.

[35] F. Bernardeau and R. van de Weygaert, "A new method for accurate estimation of velocity field statistics," *Monthly Notices of the Royal Astronomical Society*, vol. 279, p. 693–711, Mar. 1996.

[36] K. M. Gorski, E. Hivon, and B. D. Wandelt, "Analysis issues for large cmb data sets," 1998.

[37] K. P. Drake and G. B. Wright, "A fast and accurate algorithm for spherical harmonic analysis on healpix grids with applications to the cosmic microwave background radiation," *Journal of Computational Physics*, vol. 416, p. 109544, 2020.

[38] K. M. Górski, E. Hivon, A. J. Banday, B. D. Wandelt, F. K. Hansen, M. Reinecke, and M. Bartelmann, "Healpix: A framework for high-resolution discretization and fast analysis of data distributed on the sphere," *The Astrophysical Journal*, vol. 622, p. 759, apr 2005.

[39] M. R. Calabretta and B. F. Roukema, "Mapping on the HEALPix grid," *Monthly Notices of the Royal Astronomical Society*, vol. 381, pp. 865–872, 10 2007.

[40] D. J. Griffiths, *Introduction to electrodynamics*. Pearson, 2013.

[41] M. Medvinsky, S. Tsynkov, and E. Turkel, "Direct implementation of high order bgt artificial boundary conditions," *Journal of Computational Physics*, vol. 376, pp. 98–128, 2019.

[42] Arfken, G. B., 1922-, and H.-J. Weber, *Mathematical methods for physicists*. Boston: Elsevier, 6th ed. ed., 2005.

[43] M. A. Aragón-Calvo, R. van de Weygaert, and B. J. T. Jones, "Multiscale phenomenology of the cosmic web," *Monthly Notices of the Royal Astronomical Society*, vol. 408, pp. 2163–2187, 10 2010.

[44] J. M. Colberg, K. S. Krughoff, and A. J. Connolly, "Intercluster filaments in a CDM Universe," *Monthly Notices of the Royal Astronomical Society*, vol. 359, pp. 272–282, 05 2005.

[45] S. Codis, D. Pogosyan, and C. Pichon, "On the connectivity of the cosmic web: theory and implications for cosmology and galaxy formation," *Monthly Notices of the Royal Astronomical Society*, vol. 479, pp. 973–993, 06 2018.

[46] Angelinelli, M., Ettori, S., Vazza, F., and Jones, T. W., "Proprieties of clumps and filaments around galaxy clusters," *AA*, vol. 653, p. A171, 2021.

[47] L. A. Pereyra, M. A. Sgró, M. E. Merchán, F. A. Stasyszyn, and D. J. Paz, "Detection and analysis of cluster–cluster filaments," *Monthly Notices of the Royal Astronomical Society*, vol. 499, pp. 4876–4886, 10 2020.

[48] M. Jaber, M. Peper, W. A. Hellwing, M. A. Aragón-Calvo, and O. Valenzuela, "Hierarchical structure of the cosmic web and galaxy properties," *Monthly Notices of the Royal Astronomical Society*, vol. 527, pp. 4087–4099, 11 2023.

[49] R. K. Sheth and R. van de Weygaert, "A hierarchy of voids: much ado about nothing," *Monthly Notices of the Royal Astronomical Society*, vol. 350, p. 517–538, May 2004.

[50] R. Scoccimarro, "The bispectrum: From theory to observations," *The Astrophysical Journal*, vol. 544, p. 597, dec 2000.

[51] Y. Amoura, N. E. Drakos, A. Berrouet, and J. E. Taylor, "Cluster assembly times as a cosmological test," *Monthly Notices of the Royal Astronomical Society*, vol. 508, pp. 100–117, 09 2021.

[52] M. Cautun, R. van de Weygaert, and B. J. T. Jones, "Nexus: tracing the cosmic web connection," *Monthly Notices of the Royal Astronomical Society*, vol. 429, p. 1286–1308, Dec. 2012.

Appendices

A Appendix A: Cosmic Atlas

Each of the clusters was examined by mass distribution and flow at five different redshifts. The following Appendix is structured to highlight those features at radii of 10 Mpc and 5 Mpc respectively.

A.1 Cluster 1

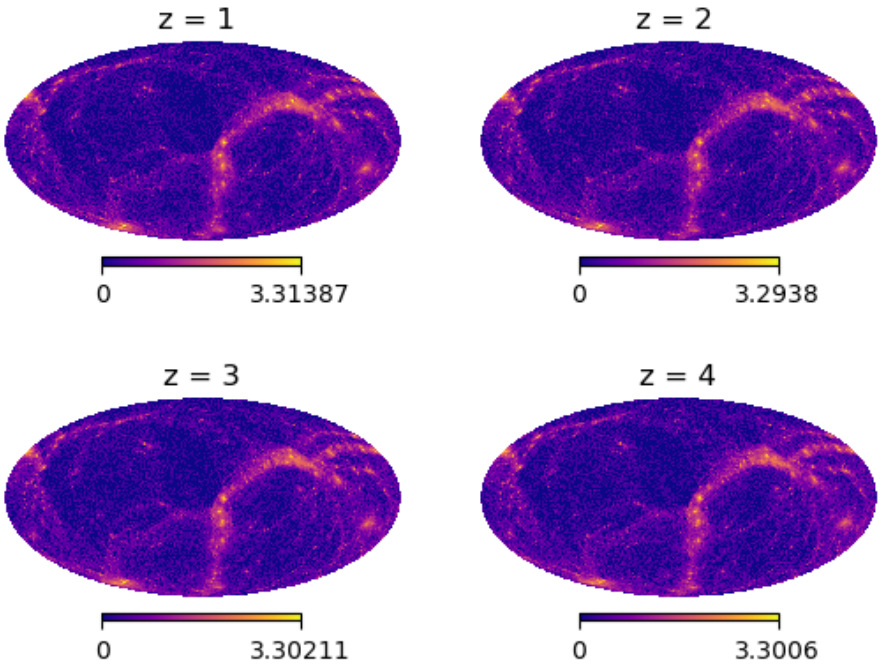

Figure 28: Mass distribution around Cluster 1 over redshift $z = 1$ to $z = 5$ at 10 Mpc radius from the center.

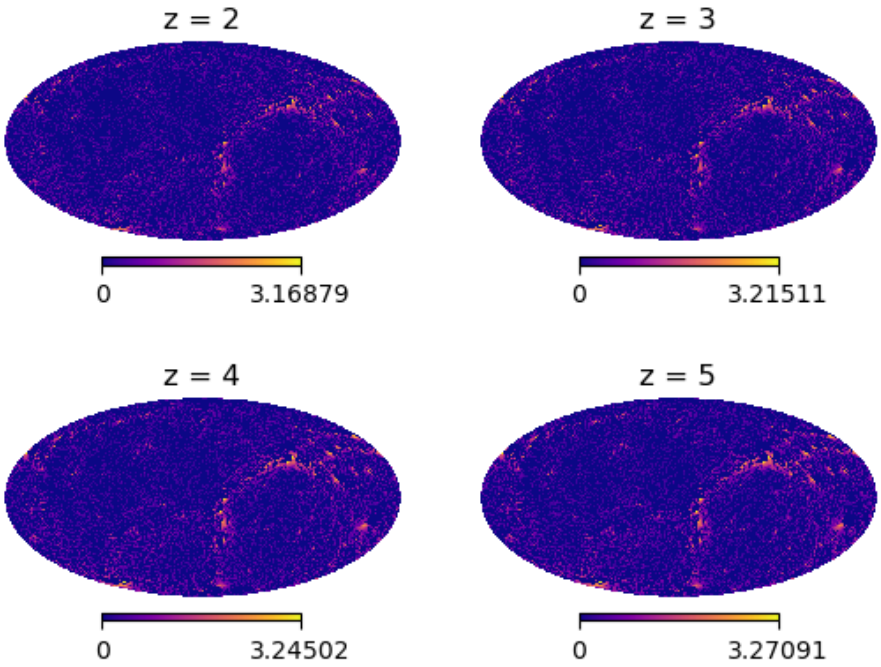

Figure 29: Mass distribution around Cluster 1 over redshift $z = 1$ to $z = 5$ at 5 Mpc radius from the center.

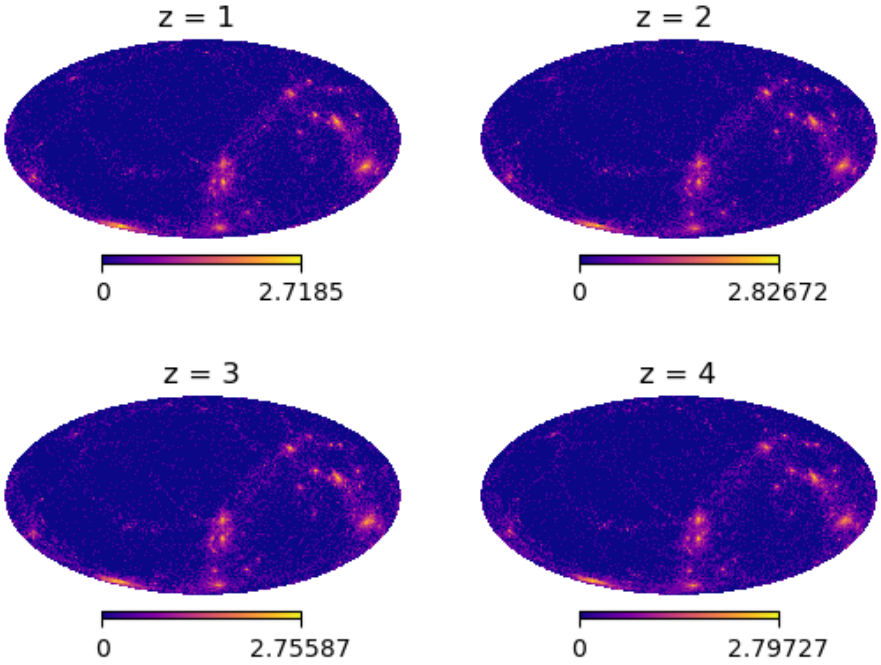

Figure 30: Influx distribution around Cluster 1 over redshift $z = 1$ to $z = 5$ at 10 Mpc radius from the center.

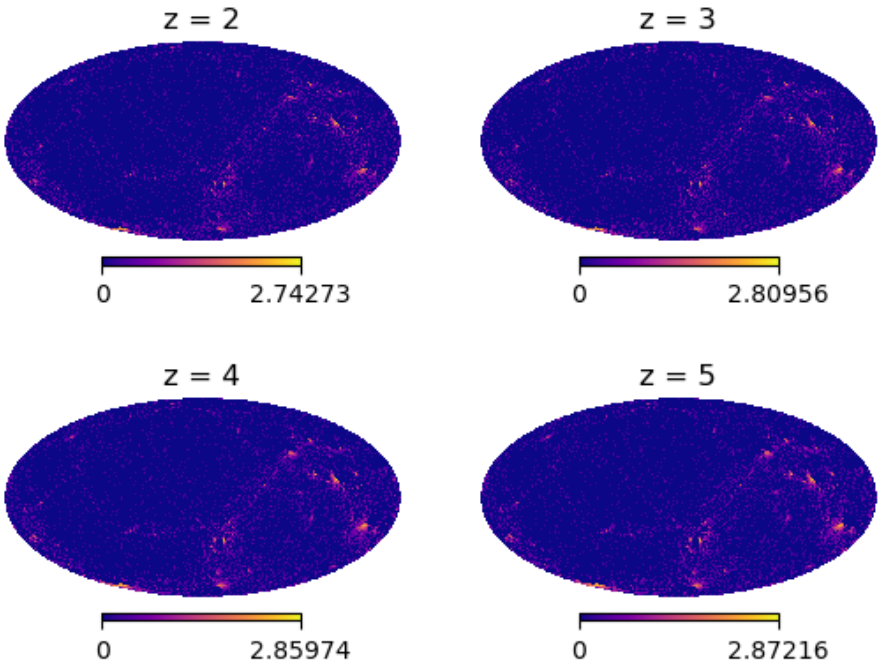

Figure 31: Mass distribution around Cluster 1 over redshift $z = 1$ to $z = 5$ at 5 Mpc radius from the center.

A.2 Cluster 2

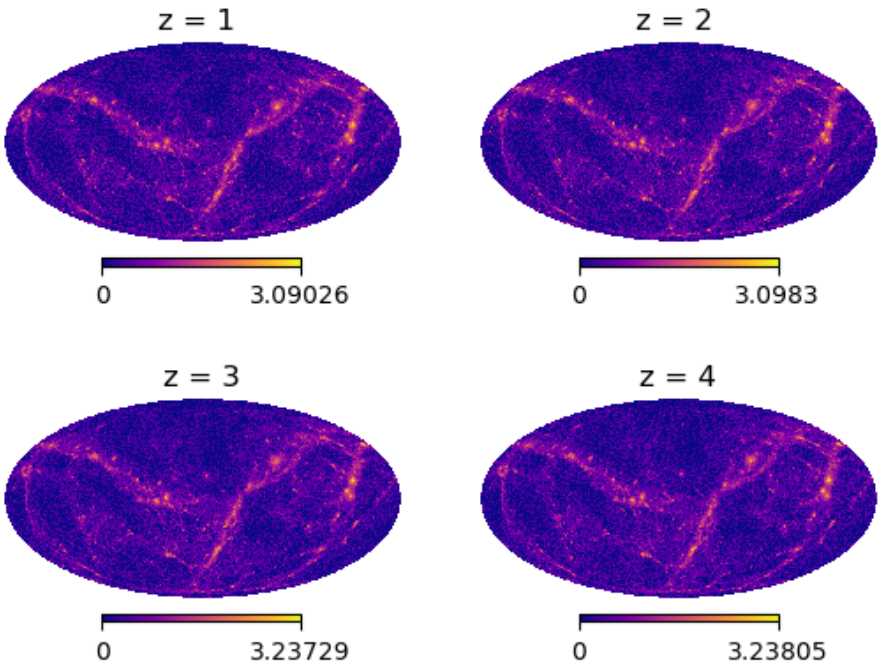

Figure 32: Mass distribution around Cluster 2 over redshift $z = 1$ to $z = 5$ at 10 Mpc radius from the center.

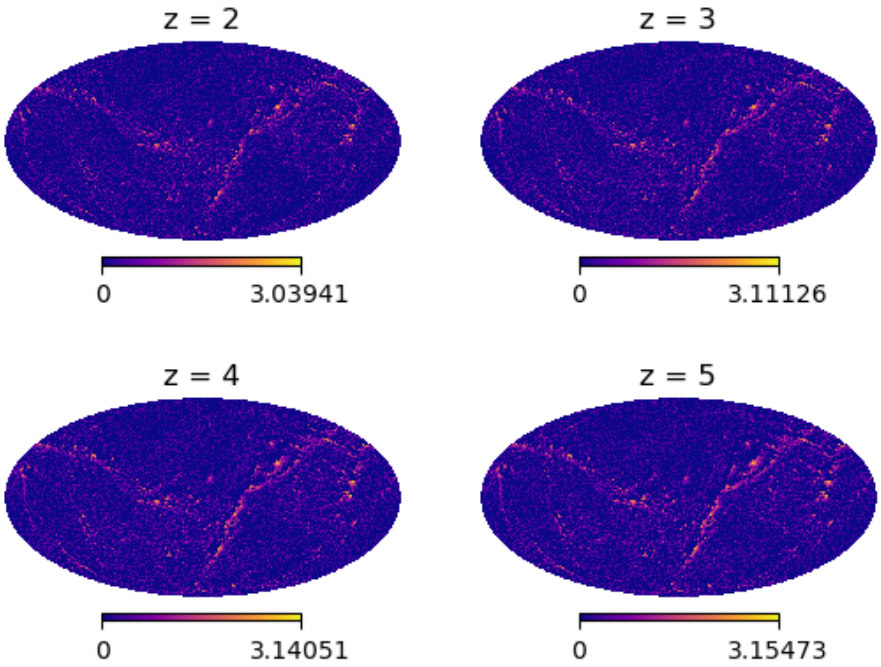

Figure 33: Influx distribution around Cluster 2 over redshift $z = 1$ to $z = 5$ at 10 Mpc radius from the center.

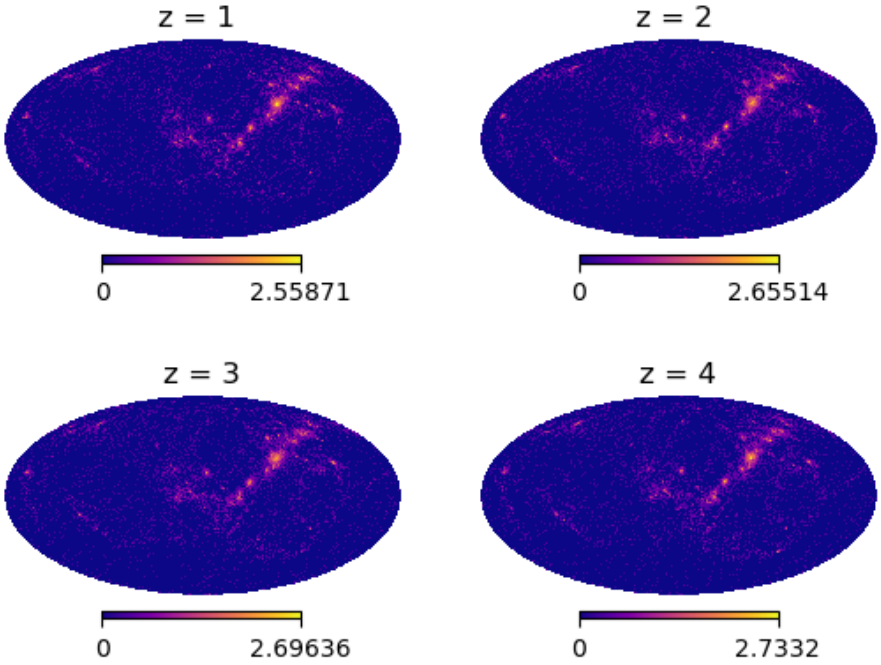

Figure 34: Mass distribution around Cluster 2 over redshift $z = 1$ to $z = 5$ at 5 Mpc radius from the center.

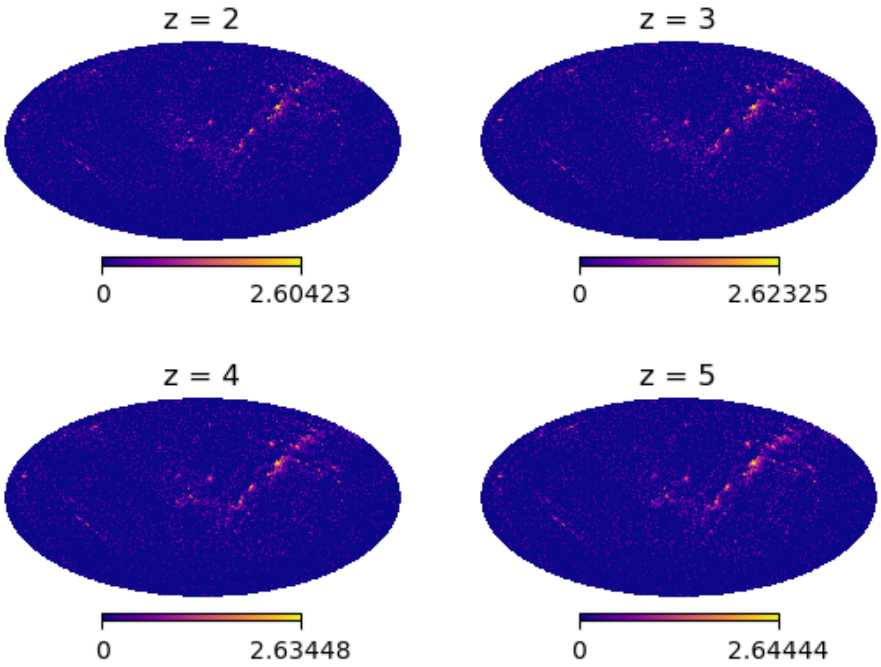

Figure 35: Influx distribution around Cluster 2 over redshift $z = 1$ to $z = 5$ at 5 Mpc radius from the center.

A.3 Cluster 3

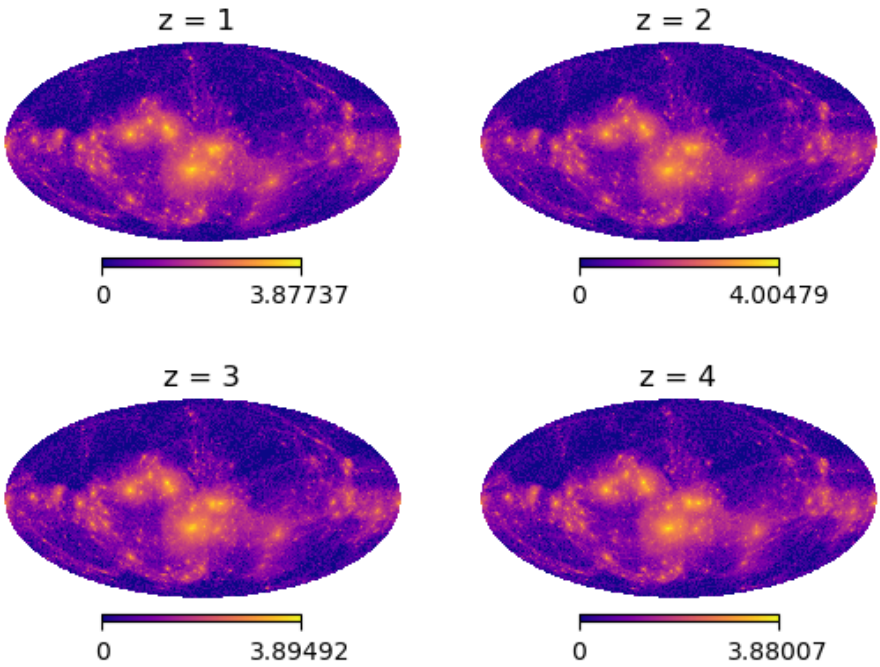

Figure 36: Mass distribution around Cluster 3 over redshift $z = 1$ to $z = 5$ at 10 Mpc radius from the center

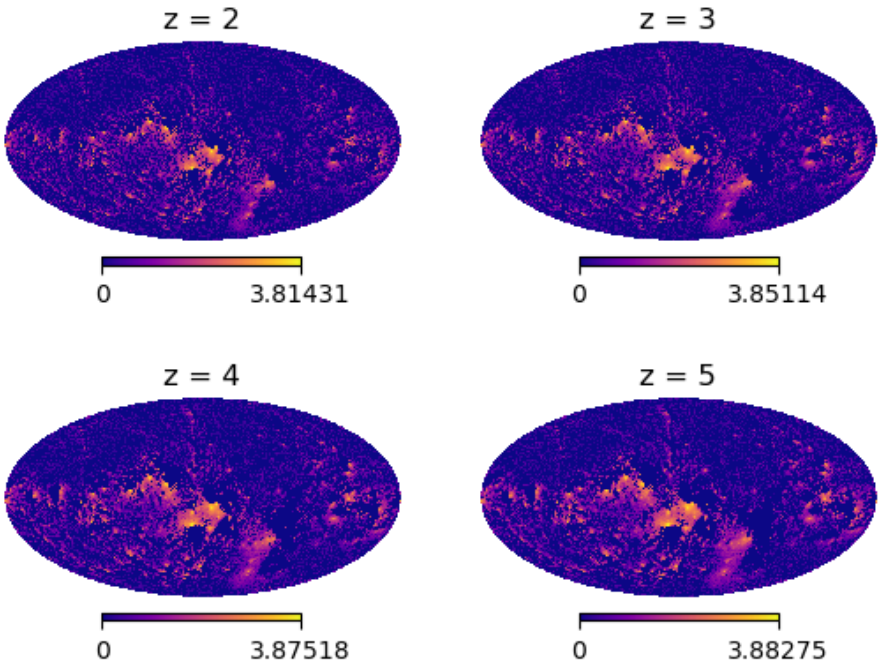

Figure 37: Influx distribution around Cluster 3 over redshift $z = 1$ to $z = 5$ at 10 Mpc radius from the center.

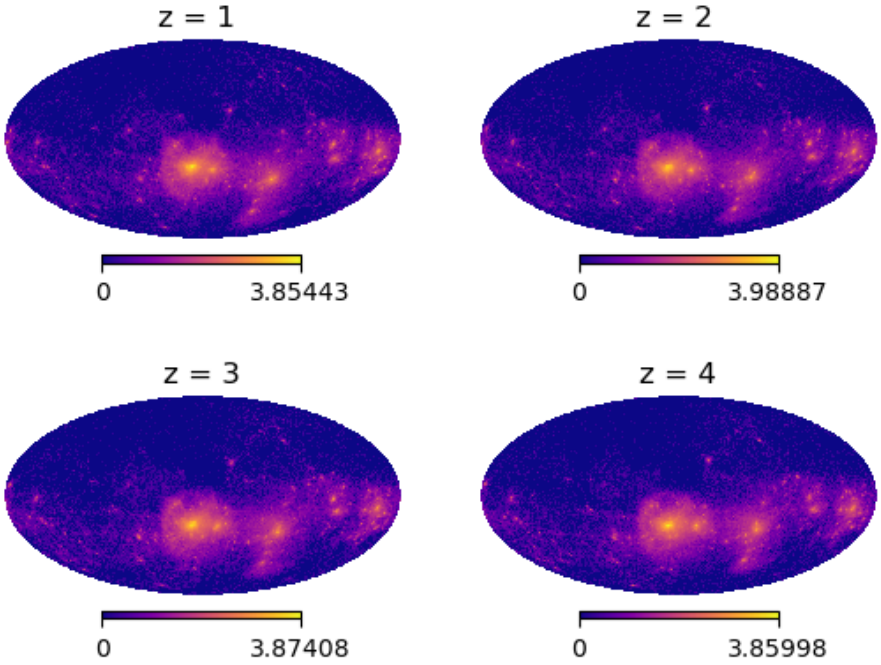

Figure 38: Mass distribution around Cluster 3 over redshift $z = 1$ to $z = 5$ at 5 Mpc radius from the center.

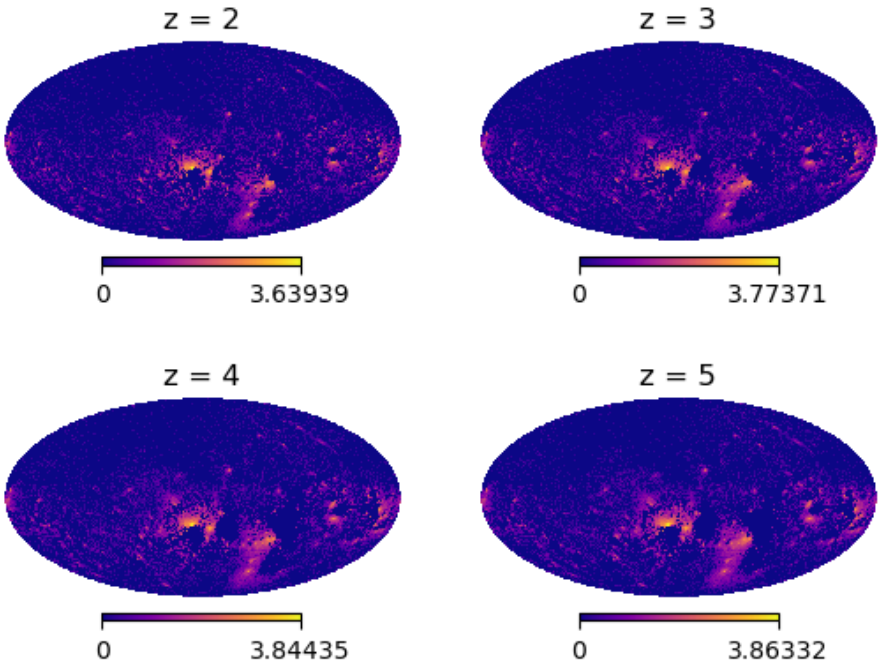

Figure 39: Influx distribution around Cluster 2 over redshift $z = 1$ to $z = 5$ at 5 Mpc radius from the center.

A.4 Cluster 4

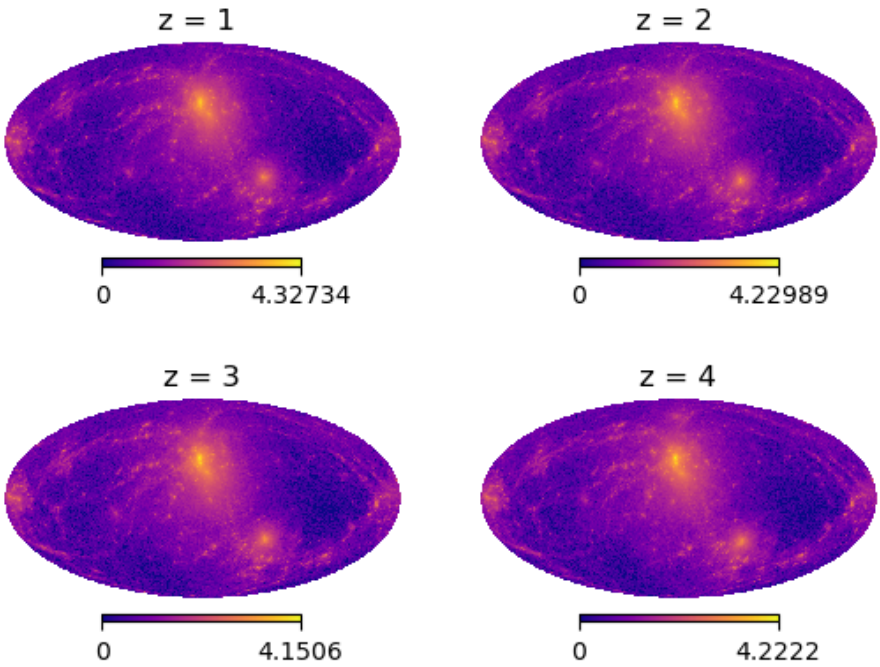

Figure 40: Mass distribution around Cluster 4 over redshift $z = 1$ to $z = 5$ at 10 Mpc radius from the center

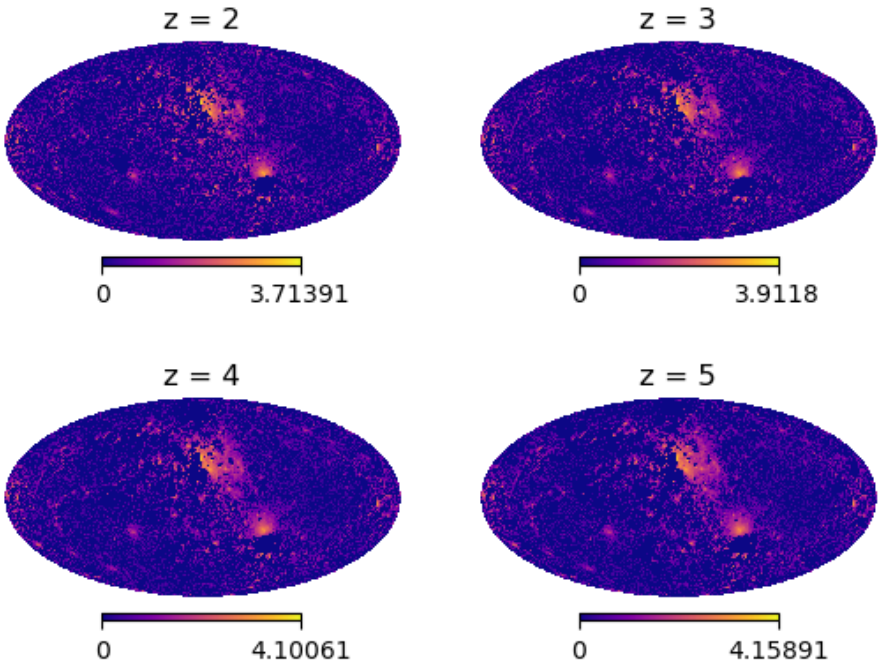

Figure 41: Influx distribution around Cluster 4 over redshift $z = 1$ to $z = 5$ at 10 Mpc radius from the center

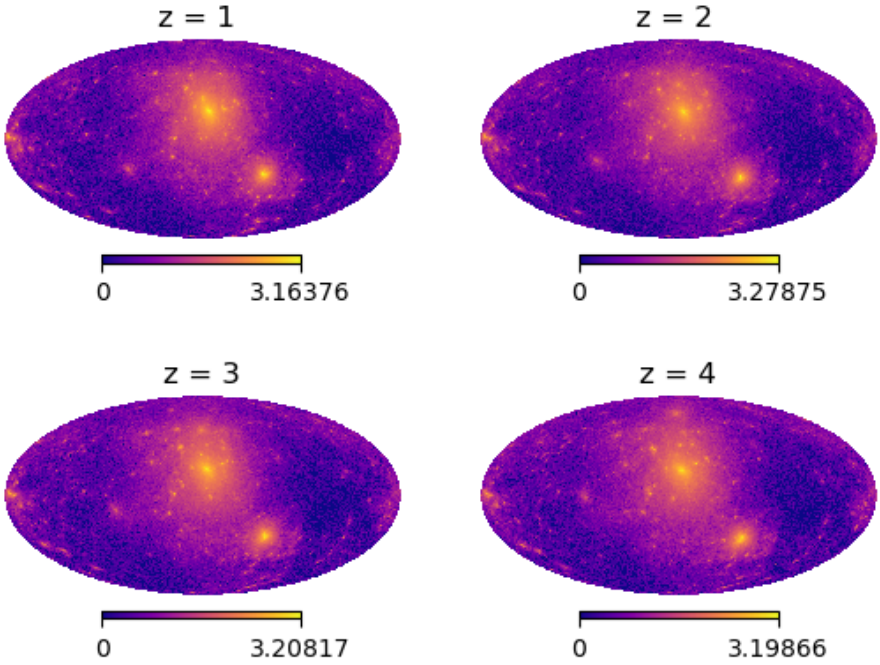

Figure 42: Mass distribution around Cluster 4 over redshift $z = 1$ to $z = 5$ at 5 Mpc radius from the center

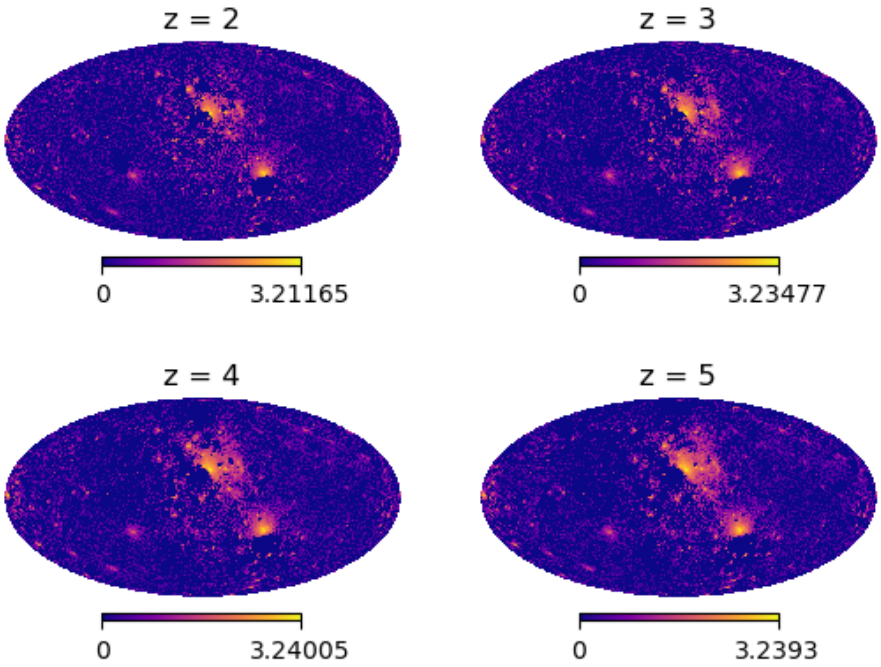

Figure 43: Influx distribution around Cluster 4 over redshift $z = 1$ to $z = 5$ at 5 Mpc radius from the center.

A.5 Cluster 5

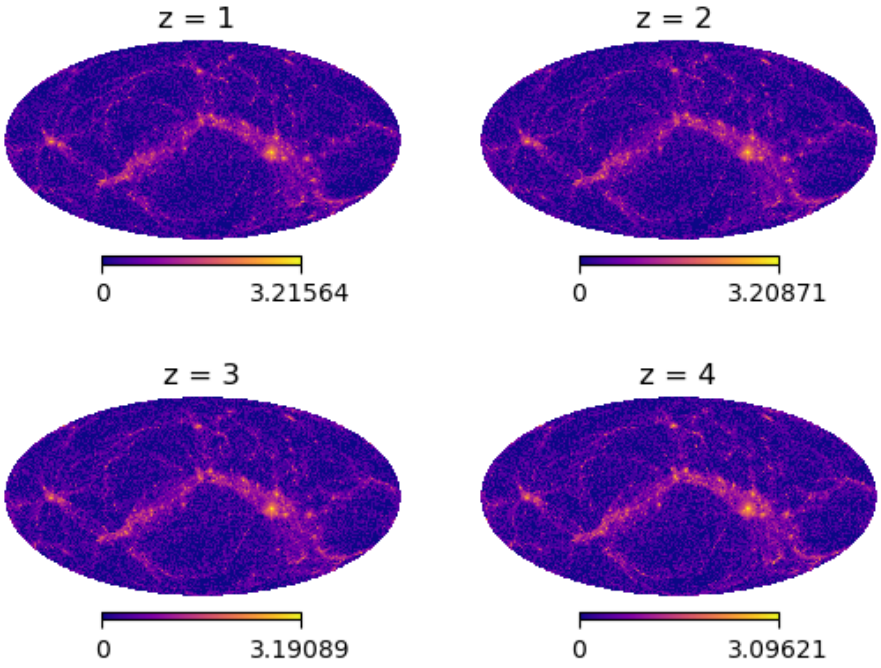

Figure 44: Mass distribution around Cluster 5 over redshift $z = 1$ to $z = 5$ at 10 Mpc radius from the center.

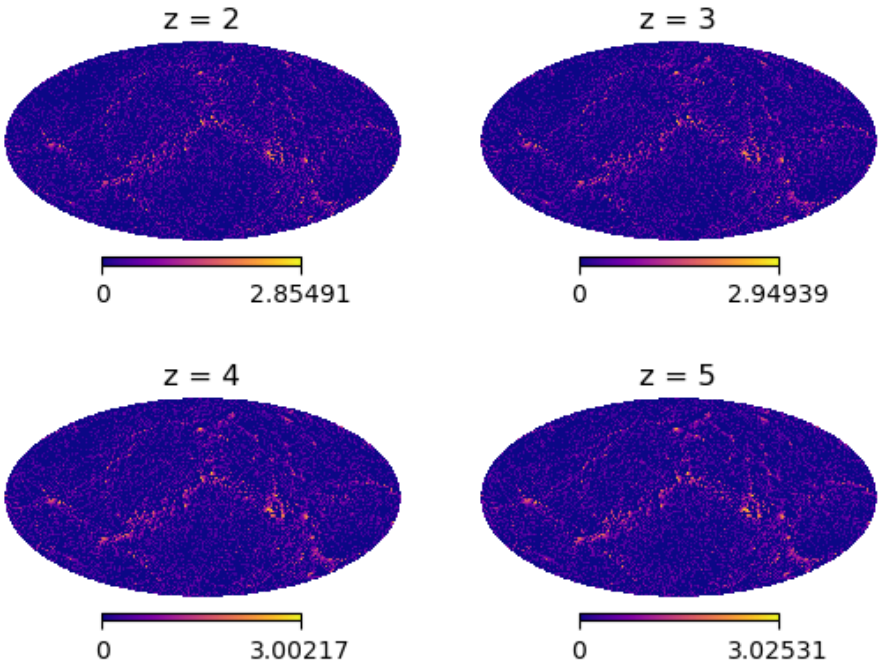

Figure 45: Influx distribution around Cluster 5 over redshift $z = 1$ to $z = 5$ at 10 Mpc radius from the center.

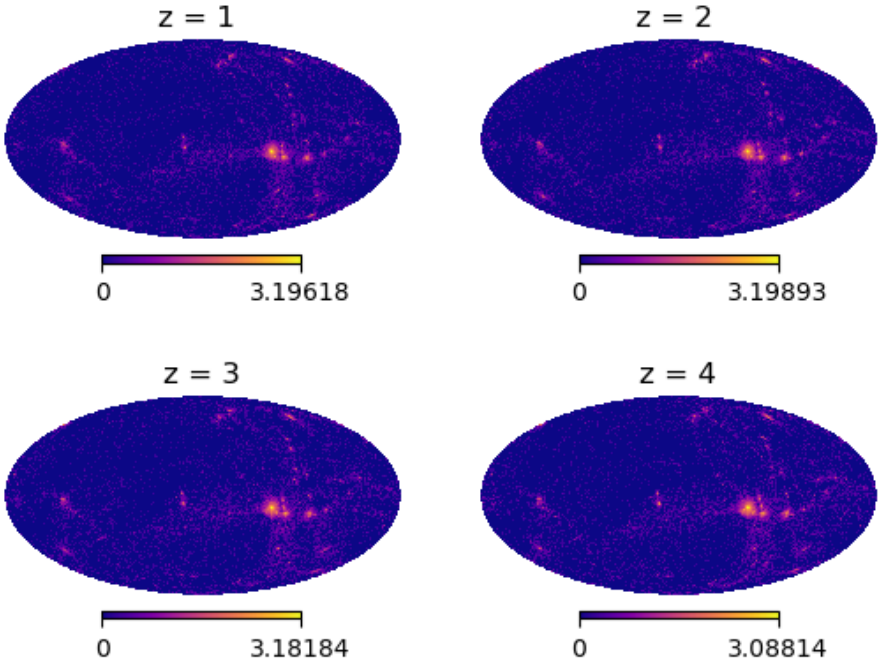

Figure 46: Mass distribution around Cluster 2 over redshift $z = 1$ to $z = 5$ at 5 Mpc radius from the center

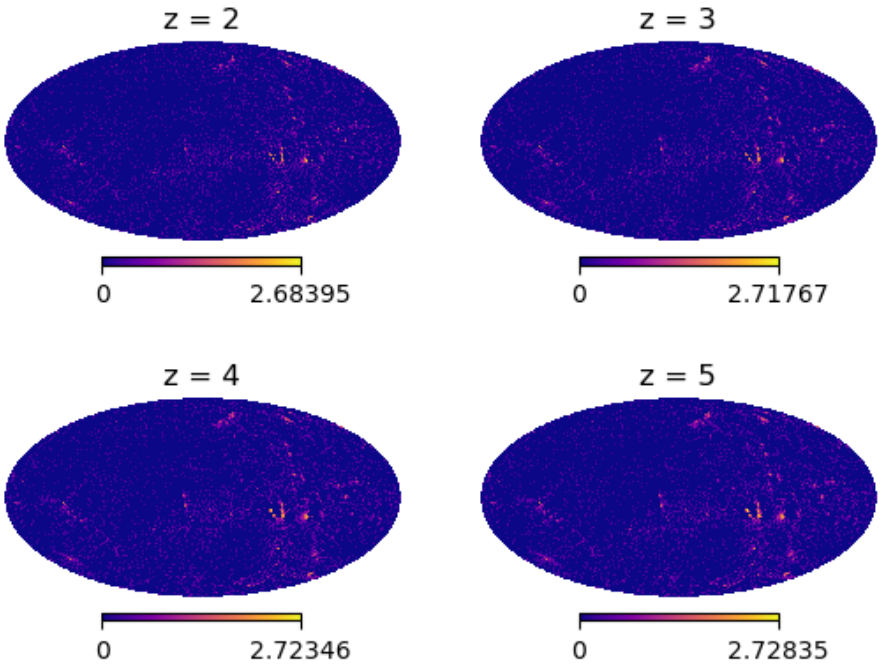

Figure 47: Influx distribution around Cluster 2 over redshift $z = 1$ to $z = 5$ at 5 Mpc radius from the center.

B Filament and void contribution to matter flow

The contributions from filaments and voids to the matter flow around clusters were examined separately over five different redshifts. The results for the remaining three clusters, complementing figures 50 and 26, are highlighted below.

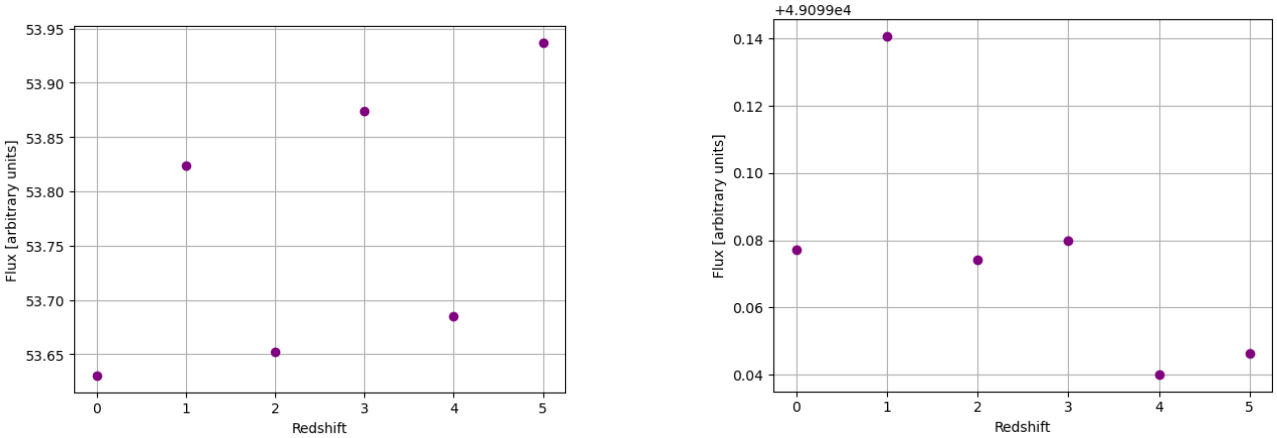

((**a**)) Void contribution

((**b**)) Filament contribution

Figure 48: Comparison between the mass inflow from the voids and the filaments within Cluster 2.

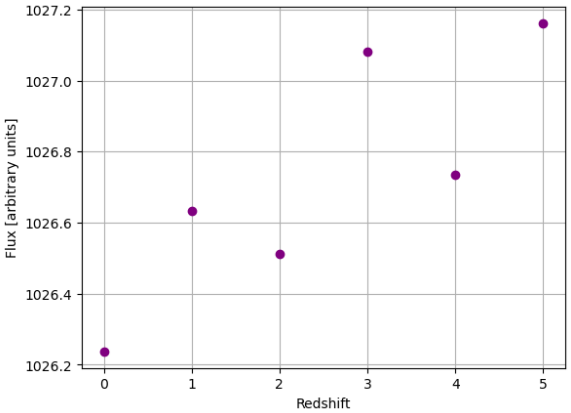

((**a**)) Void contribution

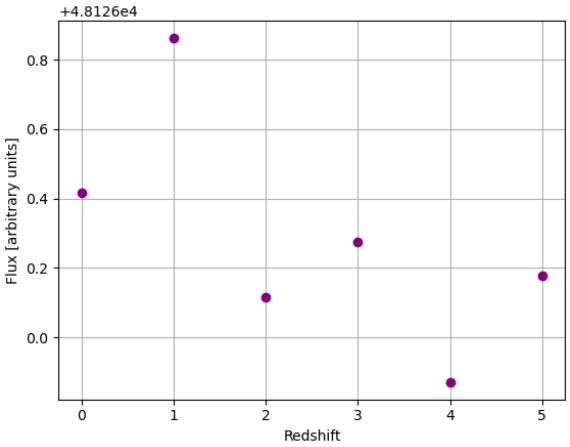

((**b**)) Filament contribution

Figure 49: Comparison between the mass inflow from the voids and the filaments within Cluster 4.

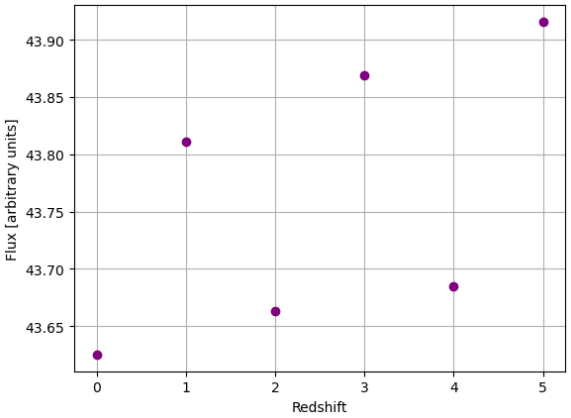

((**a**)) Void contribution

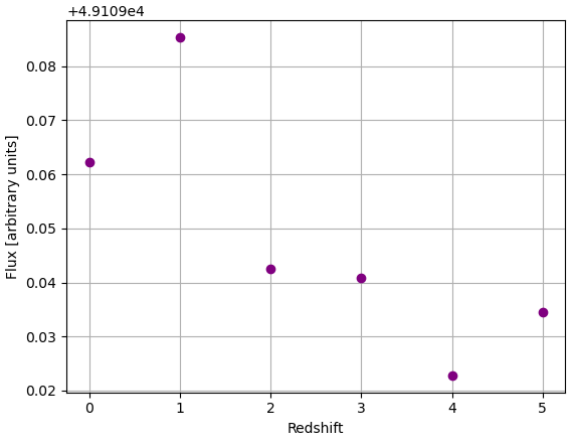

((**b**)) Filament contribution

Figure 50: Comparison between the mass inflow from the voids and the filaments within Cluster 2.